Physics of Fluids

RESEARCH ARTICLE | MARCH 12 2024

Formation and propagation characteristics of a weak shock wave in maglev tube

Special Collection: Flow and Civil Structures

Kai-Wen Wang (王凯文) ; Xiao-Hui Xiong (熊小慧) ; Chih-Yung Wen (溫志湧) ;
Guang Chen (陈光) ✉ ; Xi-Feng Liang (梁习锋) ; Hua-Kun Huang (黄华坤) ; Jia-Bin Wang (王家斌)

Physics of Fluids 36, 036120 (2024)
https://doi.org/10.1063/5.0196330

Formation and propagation characteristics of a weak shock wave in maglev tube

Cite as: Phys. Fluids **36**, 036120 (2024); doi: 10.1063/5.0196330
Submitted: 6 January 2024 · Accepted: 23 February 2024 ·
Published Online: 12 March 2024

Kai-Wen Wang (王凯文),[1,2,3,4] Xiao-Hui Xiong (熊小慧),[1,2,3,4] Chih-Yung Wen (溫志湧),[5] Guang Chen (陈光),[1,2,3,4,a)] Xi-Feng Liang (梁习锋),[1,2,3,4] Hua-Kun Huang (黄华坤),[5] and Jia-Bin Wang (王家斌)[1,2,3,4]

AFFILIATIONS

[1] The State Key Laboratory of Heavy-Duty and Express High-power Electric Locomotive, Central South University, Changsha 410075, China
[2] Key Laboratory of Traffic Safety on Track (Central South University), Ministry of Education, School of Traffic and Transportation Engineering, Central South University, Changsha 410075, China
[3] Joint International Research Laboratory of Key Technology for Rail Traffic Safety, Central South University, Changsha 410075, China
[4] National & Local Joint Engineering Research Center of Safety Technology for Rail Vehicle, Central South University, Changsha 410075, China
[5] The Hong Kong Polytechnic University, Department of Aeronautical and Aviation Engineering, Kowloon, Hong Kong, China

Note: This paper is part of the special topic, Flow and Civil Structures.
[a)] **Author to whom correspondence should be addressed:** gszxcgsq@163.com

ABSTRACT

The propagation of the weak shock wave (WSW) to the tunnel exits and their radiation as micro-pressure waves (MPWs) may cause sonic booms or structural resonance of buildings, posing potential hazards to humans, animals, and buildings in the exit's environment. The characteristics of the WSW and sonic booms of a maglev train/tube coupling model were studied based on the two-dimensional axisymmetric unsteady Reynolds average Navier–Stokes turbulence model. In the later stage of a MPW, the formation mechanism, geometry, and kinematic characteristics of compressible vortex rings (CVRs) were systematically analyzed. The inertial effect causes the initial wavefront to gradually transition from a Gaussian-shape waveform to a triangular waveform during its propagation, eventually coalescing into a WSW. The overpressure, density jump, and shock Mach number at the WSW location all increase with the increasing train speed, while the WSW thickness decreases accordingly. The formation distance of the WSW is inversely proportional to the amplitude of the initial wavefront gradient, and the WSW directly causes the occurrence of the exit sonic boom. The MPW amplitude has significant directionality with a largest value in the axial direction. Within the speed range of 450–700 km/h, the sound pressure level of the MPW exceeds the hearing threshold and even reaches the feeling threshold. The evolution of CVRs includes primary CVR, secondary CVR, and Kelvin–Helmholtz vortices. Primary CVR has the greatest impact on the axial MPW among them. The occurrence of CVRs will cause a second small noise level other than the sonic boom.

I. INTRODUCTION

The propagating compressional wave generated by the train entering the tunnel splits into two branches when it reaches the exit end. One branch reflects back to the tunnel under the influence of the exterior atmospheric pressure, forming an expansion wave.[1,2] The other one emits micro-pressure waves (MPWs) at the tunnel exit, which then radiate into the surrounding environment in the form of impulse waves.[3–5] The phenomena of sonic booms and the creaking doors and windows of surrounding buildings occur when the MPW amplitude is large enough.[3] The MPW amplitude is usually proportional to the wavefront gradient at the tunnel exit.[6] Hieke *et al.*[7] suggested that a wavefront gradient greater than 40 kPa/s at the exit can produce a strong audible sonic boom. Within the speed range of wheeled railway trains, the wavefront gradient at the tunnel exit is proportional to the cube of the train speed.[8] Interestingly, this power exponent jumps to an astonishing 4.99 with the expected speed of maglev trains reaching up to 0.5M ($M = V_t/C_o$, where V_t represents the train speed and C_o represents the speed of sound).[9] Considering the potential negative effects caused by the infrasonic and audible components of MPW on humans, animals, and buildings near the tunnel exit, it is of great significance to further explore the causes and characteristics of sonic booms.

The sonic boom caused by a maglev train entering a tunnel reminds gas dynamicists of the classic shock tube problem driven by a piston. The maglev train can be compared to a leaky piston, where the propagating compressional wave continuously propagates forward within a finite tube.[10] The wavefront gradient is affected by both inertial steepening and friction effects.[11] Inertial steepening tends to increase the wavefront gradient. Because the sound speed in the pressurized air behind the wave is slightly greater than that in the unpressurized air ahead of the wave, this causes the rear wave tending to catch up with the front wave, making the nonlinear steepening of the wavefront profile. Friction effects, due to wall friction, tend to reduce the wavefront gradient. Since the maglev tube adopts slab-track, inertial steepening is bound to outweigh the losses from friction effects. Therefore, the propagating compressional wave will coalesce into a weak shock wave (WSW) that is different from that in gas dynamics, which is the main cause of sonic booms.[12,13] This WSW has also been observed in a train tunnel simulator using double-exposure holographic interferometry.[12] The overpressure at the WSW location generated by a flat-headed piston traveling at 270 km/h through a tube with a blockage ratio of 0.2 is 1.8 kPa, corresponding to a shock Mach number of 1.008. Rivero *et al.*[13] proposed a one-dimensional prediction model for the WSW induced by propagating compressive waves based on the characteristic line method. The study showed that the formation distance of the WSW is determined by the initial wavefront and the initial wavefront gradient. Additionally, the impacts of the heat transfer and friction on the formation distance of the WSW are relatively small. Therefore, it is crucial to understand the formation mechanism of the WSW, namely, the nonlinear steeping of the wavefront, as well as its physical characteristics and propagation laws.

The distortion process of the wavefront is related to many factors, including the shape and amplitude of the initial wavefront and the friction effect in the tunnel.[14,15] The characteristics of the initial wavefront depend on factors such as the shape of the train head,[2] the tunnel hood structure,[16,17] and the speed of the train.[9] The three common shapes of train heads: conical, parabolic, and elliptical heads have different influences on the amplitude and gradient of the initial wavefront due to their different streamlined heads.[2] The parabolic head is more like the shape of the beak in bionics and has superior effects. On this basis, Miyachi *et al.*[18] proposed a multistep train nose and explored its optimization effect on the multi-stage flow field inside the tube. Experimental verification showed that this multi-step nose can reduce the MPW amplitude by more than 5%. Zhang *et al.*[16] designed a novel vented tunnel hood, which can reduce the MPW amplitude at the 20 m away the exit by up to 84% through the reasonable combination of vented hoods. Additionally, Zhang *et al.*[17] also envisioned a novel arch lattice-shell of enlarged cross section hoods, which can reduce the MPW amplitude at the 20 m away the exit by 74% compared to the maglev tunnel without this structure design.

There have also been many discussions on the impact of friction effects on the evolution of initial wavefronts in the tunnel. Vardy *et al.*[19,20] pioneered the exploration of the effects of inertial effects, friction effects, and ballast tracks on the propagation of simple waves in tube, and further developed a non-steady friction model for pipeline flow by considering ballasts as a series of Helmholtz resonators. Miyachi *et al.*[21] explored the effect of nonlinear and non-steady friction on wavefront steeping and obtained the relationship between wavefront steeping and initial wavefront. In engineering applications, the Nuremberg-Ingolstadt railway in Germany adopted absorbers on the tunnel wall to dissipate the energy of the propagating wavefront and suppress the wavefront steeping.[22] Through the comparison of experimental data and one-dimensional models, the unsteady friction model achieves accurate prediction of wavefront attenuation under the action of absorbers. Recently, Wang *et al.*[14] explored the influence of different initial wavefronts on the evolution of wavefronts and further improved the role of inertia and friction on the evolution of wavefronts. Through one-dimensional model simulation, Wang *et al.*[14] obtained a critical tunnel length, which is the tunnel length corresponding to the maximum wavefront gradient. This result is of great benefit to the conceptual design of railway tunnels. Moreover, Iyer *et al.*[15] explored the effects of blockage ratio and train speed on the wavefront steeping through one-dimensional unsteady friction equations and obtained the critical tunnel length through the steeping ratio of the wavefront. The previous research is of great help in understanding the wavefront evolution process in railway tunnels. Generally, short tunnels have little effect on the wavefront steepening because the time for wave propagation is relatively short. However, for the maglev tube, the amplitude and gradient of the initial wavefront will increase sharply, resulting in a significant reduction in the critical tunnel length. Moreover, the steepening process of the wavefront in the maglev tube, the physical phenomenon of the formation of the WSW, and the subsequent sonic boom problems have not been well explored to date.

The steepening process of the wavefront causes the wavefront gradient to gradually increase and reach a critical value during propagation. Although the wavefront gradient decreases significantly at the tunnel exit, the impact of the emitted MPW on the exit environment cannot be ignored. Previously, scholars explored the radiation solid angle model of circular tube and established the relationship between MPW and the exit wavefront gradient.[23] However, the exit terrain can change the radiation path of MPW. Therefore, Miyachi *et al.*[23] developed a MPW prediction model based on the linear acoustic theory. The directionality and terrain effects of MPW in an open space have been fully studied. Wang *et al.*[24] studied the impact of a two-dimensional perforated duct on the characteristics of MPW and found that the perforated area can effectively reduce the exit wavefront gradient. The perforated duct significantly reduces the MPW amplitude by interfering with MPW and changing its radiation path. Moreover, Wang *et al.*[25] explored the influence of tunnel portals in cuttings on the radiation characteristics of MPW. The research showed that these cuttings would have a strong impact on MPW with elliptical radiation, with obvious columnar behavior in deep and narrow cuttings, and the MPW tail of narrow cuttings exhibited oscillations. The above studies analyzed the amplitude and waveform of MPW from the perspective of temporal pressure. However, current MPW evaluation standards include the impulse amplitude and the acoustic evaluation[11,26] (as summarized in Fig. 1). For example, the impulse amplitude in Japan, South Korea, and China adopts a single point MPW amplitude as the threshold. In Germany, the acoustic standard sets the threshold based on the C-weighted MPW sound peak value, as stipulated in European directive 2003/10/EC.[27] However, the spectral characteristics of MPW have not been fully explored to date, especially in relation to human hearing,[28] which is important for understanding the generation of sonic boom phenomena.

The existing MPW research only explores the transient process of MPW impulse waves. Interestingly, in the later stage of MPW, a series

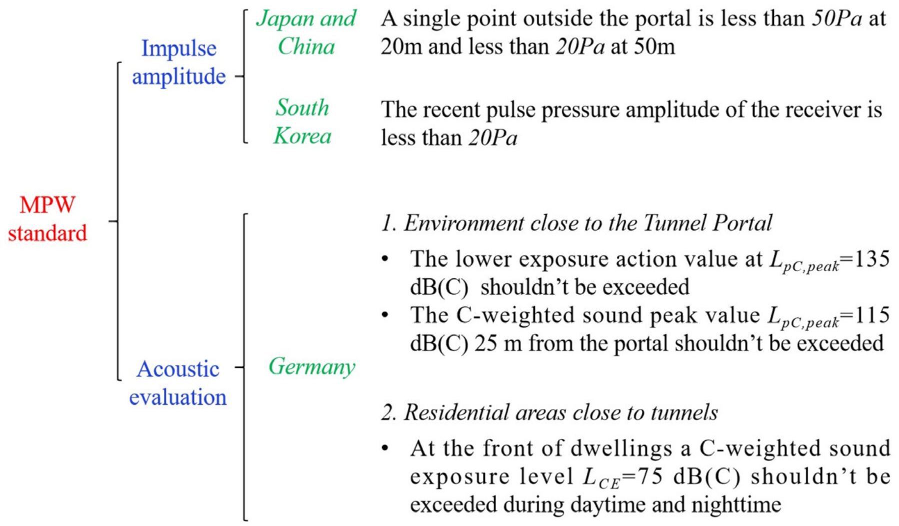

A single point outside the portal is less than *50Pa* at 20m and less than *20Pa* at 50m

The recent pulse pressure amplitude of the receiver is less than *20Pa*

1. Environment close to the Tunnel Portal

- The lower exposure action value at $L_{pC,peak}$=135 dB(C) shouldn't be exceeded
- The C-weighted sound peak value $L_{pC,peak}$=115 dB(C) 25 m from the portal shouldn't be exceeded

2. Residential areas close to tunnels

- At the front of dwellings a C-weighted sound exposure level L_{CE}=75 dB(C) shouldn't be exceeded during daytime and nighttime

FIG. 1. Summary of MPW standard in terms of the impulse amplitude and the acoustic evaluation.[11,26]

of vortex ring structures are generated at the joint of tube and flange and develop downstream (as shown in Fig. 21). Vortex ring is a fascinating fluid dynamic phenomenon in nature, with vortex lines forming a closed loop.[29] Vortex rings usually appear in the tail of aircraft, volcanic eruptions, pipeline jets, and smoke rings.[30,31] Meanwhile, the propagating compression wave also generates vortex ring structures after radiating from the tube. The compressible vortex ring (CVR) generated by a shock tube is different from the incompressible vortex ring generated by a piston, as the vortex ring passes through areas with significant changes in air density. Based on the difference in shock Mach number (M_s), CVRs are classified as: shock-free CVRs ($M_s < 1.43$), embedded shock CVRs ($1.43 < M_s < 1.6$), embedded shock CVRs, and their front contrarotation CVRs ($M_s > 1.6$).[29] Moreover, the evolution of CVRs usually has three stages: a rapid growth stage, a pinch-off stage, and a free development stage.[32] Therefore, understanding the generation mechanism and evolution process of CVRs at the exit of a maglev tube is helpful to understand the development process of the post-stage of MPW.

In this study, we focus on the formation and propagation characteristics of the WSW in the maglev tube and clarify the relationship between the WSW and sonic booms. The rest of this article is organized as follows: Section II details the numerical calculation method, grid strategy, solution parameter settings, and numerical method validation. Section III discusses the initial wavefront characteristics and predicts the formation distance of WSW. Additionally, the spectral characteristics, directivity, evolution process, acoustic evaluation, and noise protection of MPW are fully discussed. The formation mechanism, geometry, and kinematics characteristics of CVRs are quantitatively analyzed. Finally, concluding remarks are provided in Sec. IV.

II. NUMERICAL METHOD

A. Geometric configuration and computational conditions

The 1:97 scaled experimental model conducted in the Railway Technical Research Institute of Tokyo (RTRI)[33] is considered here, which remains the identical characteristic and the cross-sectional area of the Yamanashi Maglev Test Line. To explore the evolution of wavefront steepening in a long tube and save solution resources, a two-dimensional (2D) axisymmetric train/maglev tube system is adopted in current research. With the radius of the axisymmetric train ($d = 34.6$ mm) as the characteristic length, the details of the simulation model and the computational boundary are reported in Fig. 2(c) and Table I. A rectangular coordinate system is established with the origin at the rotation axis at the entrance of the tube, and the x and y directions are along the streamwise and spanwise direction, respectively. Figures 2(a) and 2(b) depict the overall parameters of the maglev train and the tube. The total length of the maglev train L_{tr} is 37.57 d, which represents the length of 5-car formations, of which the streamlined length L_1 is 3 d. The total length (L_{tu}) and radius (R) of the maglev tube are $L_{tu} = 1489.78d$ (which represents 5 km in full-scale length) and $R = 1.45d$, respectively. The corresponding blockage ratio β, defined as the ratio of the projected area of the train and the tube, is 0.12.

The initial position of the overset zone is mounted in an 84.70 d (length)×11.92 d (radius R_1) cylindrical field, as illustrated in Fig. 2(c). The top surface and inlet are arranged as the symmetrical plane and pressure inlet, respectively. The head train nose is 14.90 d (L_4) away from the tube entrance to ensure the stable quality of the initial flow field. To improve the efficiency of information exchange between the overset grid and the background grid, the overset zone adopts the same radius as the tube. In addition, the flanges are defined as non-slip walls to restore the mountainous environment near the tube. Since the MPW radiates outward from the tube exit in an approximate spherical form, a hemisphere with a radius of $R_2 = 59.59d$ is employed to simulate the outlet natural environment. Moreover, a pressure far-field condition is assigned to the outlet to avoid the wave reflection at the outlet surface. Finally, the bottom of the overset zone and the background zone are defined as axes to substitute a three-dimensional axisymmetric model akin to the experimental equipment.

B. Grid strategy and grid independence

The quadrilateral structure grids are employed in both the overset zone and the background zone. Here, the medium grid is taken as an

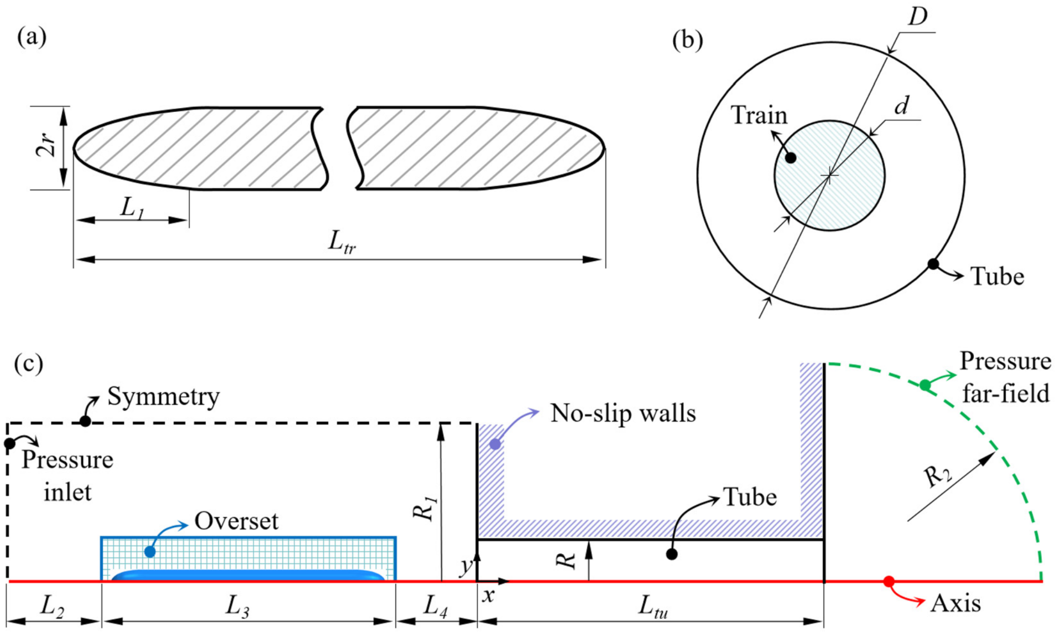

FIG. 2. Model geometry and computational domain: (a) the geometric configuration of the rotating train, (b) relative spatial positions of the train and the tube, and (c) disproportionate schematic diagram of the calculation domain of the train/maglev tube coupling system.

example to show the grids distribution in the encryption regions of the computing domain, as shown in Fig. 3. To accurately solve the evolution of the flow field around the train and the wave effect in the tube, the left air domain and the tube are progressively encrypted. The isotropic grid sizes of the overset zone, tube, refinement cylinder 1 (*RC1*), *RC2*, *RC3*, and *RC4* are 0.04 *d*, 0.04 *d*, 0.04 *d*, 0.12 *d*, 0.24 *d*, and 0.48 *d*, respectively. To adapt the radiation characteristics of MPW, the isotropic grid sizes of the refinement sphere 1 (*RS1*), *RS2*, *RS3*, and *RS4* are 0.04 *d*, 0.12 *d*, 0.24 *d*, and 0.48 *d*, respectively.

In the current study, grid independence is conducted to test the correctness of the simulation data using coarse, medium, and fine grids, and detailed parameters are provided in Table II. The three meshes with different resolutions all adopt the same construction principle and wall-normal resolution. The difference only lies in the spatial grid size of the streamwise and the spanwise direction. To accurately solve the boundary layer flow near the wall, 10 extrusion elements of prismatic layer are generated near the train surface, top of the overset zone and the tube surface. The wall-normal growth factor and the total thickness of the prismatic layer is 1.2 and 0.03 *d*, respectively. The wall-normal height of the first layer grid is 3.8×10^{-4} *d*, which ensures the average dimensionless distance, n^+, in the wall-normal direction between the first grid and the wall can be less than 1. Here, n^+ is defined as $n^+ = n\mu_\tau/\nu$, where n is the distance from the center point of the first layer grid to the wall, μ_τ is the friction velocity, and ν is the kinetic viscosity. In addition, the streamwise resolution ($\Delta l^+ = \mu_\tau \Delta l/\nu$) and spanwise resolution ($\Delta s^+ = \mu_\tau \Delta s/\nu$) are adjusted for three grids. The wall dimensions and specific parameters of the three grids with different resolutions are summarized in Table II. The above spatial encryption regions and wall grid resolution together constitute the grid strategy.

Figure 4(a) shows the internal wavefront and wavefront gradient of the tube calculated by the fine, medium, and coarse grids. To obtain a fully developed temporal wavefront, the pressure information at $x/L_{tu} = 0.5$ was employed as a comparison basis. The dimensionless time tV_t/d are adopted, where V_t is designated as an impressive train speed of 600 km/h here. The MPW sampling locations based on the polar coordinates system are presented in Fig. 4(b). The r_p and θ are specified as the distance from the sampling point to the origin and the angle between the red line and the axis, respectively. The temporal MPW at $(0.2, 0)_{MPW}$ and $(0.5, 0)_{MPW}$ location are selected for grid independence verification [see Figs. 4(c) and 4(d)]. The maximum extremum errors of the wavefront, wavefront gradient, and the MPW among three grid resolutions are 2.1%, 3.5%, and 3.3%, respectively. Considering the prediction accuracy and calculation benefit comprehensively, the medium grid strategy is adopted in the subsequent discussion.

C. Solver settings

The numerical simulations in this article utilize the finite volume method software Star-CCM+ 14.02 with an unsteady separated implicit solver. The unsteady Reynolds average Navier–Stokes

TABLE I. Dimension of the computational model and the boundaries. Symbols refer to Fig. 2.

D	L_1	L_2	L_3	L_4	L_{tr}	L_{tu}	r	R	R_1	R_2
2.89*d*	3.00*d*	29.80*d*	40.00*d*	14.90*d*	37.57*d*	1489.78*d*	0.50*d*	1.45*d*	11.92*d*	59.59*d*

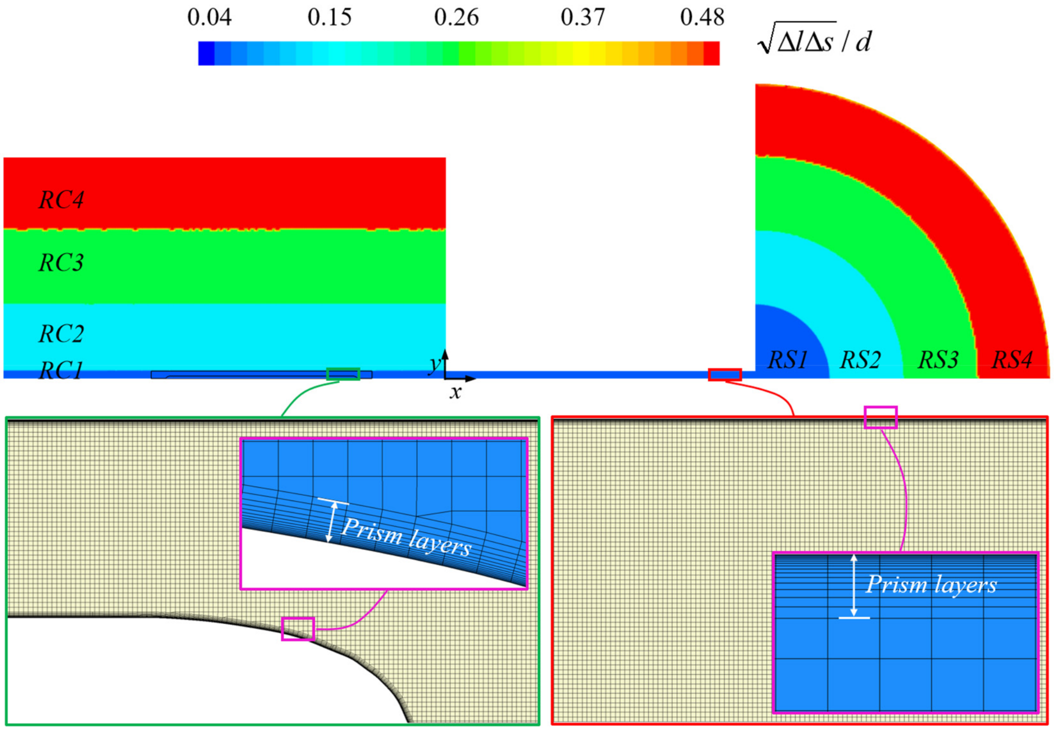

FIG. 3. Spatial encryption strategy of the grid and visualization of the local grid.

(URANS) approach is employed to solve the turbulence around the train and the propagation of wavefront inside the tube. Given the symmetrical nature of the computational model, a two-dimensional axisymmetric model[34,35] is adopted to optimize computational resources and enhance grid resolution. As the speed range of the maglev train falls within 0.37 and 0.57*M*, combined with the compression effects inside the tube, the airflow is considered compressible. Correspondingly, based on the train diameter d (34.6 mm), train speed V_t (range from 450 to 700 km/h), air density ρ (1.177 kg/m^3), and air viscosity μ (1.855×10^{-5} kg/m/s), the Reynolds number $\mathrm{Re} = \rho V_t d/\mu$ ranges from 2.7×10^5 to 4.3×10^5, which is 1/97 of the full-scale Reynolds number. In Sec. II D 3, the influence of the Reynolds number will be further analyzed. Therefore, the shear stress transport (SST) κ–ω model is adopted for the simulation, which is a hybrid turbulence model that combines the features of the standard κ–ω model and standard k–ε mode and is suitable for complex flow fields with strong shear and large Reynolds numbers.

TABLE II. Detailed spatial and boundary layer dimensions of three grids.

Grid	Object	n^+_{mean}	n^+_{max}	Δs^+_{mean}	Δs^+_{max}	Δl^+_{mean}	Δl^+_{max}	Grid number
Coarse	Train	<1.0	1.5	<350	400	<350	400	7.83×10^6
	Tube	<1.0	1.8	<450	500	<450	500	
Medium	Train	<1.0	1.5	<500	550	<500	550	4.56×10^6
	Tube	<1.0	1.8	<550	600	<550	600	
Fine	Train	<1.0	1.5	<620	700	<620	700	3.05×10^6
	Tube	<1.0	1.8	<730	820	<730	820	

To accurately solve the nonlinear steepening of wavefront inside the tube and the MPW radiation process, a meticulous grid resolution and high-precision spatial and temporal discretization scheme are required. Hence, the time advancement method employs the lower–upper symmetric Gauss–Seidel (LU-SGS) iteration method with second-order accuracy. This implicit advancement method reduces approximation decomposition error through dual-time step iteration, providing relative stability and high efficiency. Each time step involves 20 internal iterations. In the spatial discretization scheme, a hybrid MUSCL third-order/central differencing method is employed for the convective term.[36] The gradient interpolation is performed using the least-square cell-based method and combined with Min-Mod gradient limiters to enhance the interpolation accuracy and stability. A second-order expression for gradient is obtained through diffusion flux correction on internal faces. The semi-implicit method known as SIMPLE is utilized to solve the coupling problem between velocity and pressure in the governing equations. To ensure the stability and convergence of calculations, the Courant–Friedrichs–Lewy (CFL) number, defined as $\mathrm{CFL} = V_t \Delta t/\Delta s$, is maintained below 1 in the simulations. Therefore, the time step Δt for the train at different speeds is set to 0.012 d/V_t, and the total time for the maglev train to travel through the computation domain is given as $T = (L_{tu} + L_3 + L_4)/V_t$.

D. Validation of numerical results

It is necessary to conduct a comprehensive review of the prediction accuracy of the solved model, in addition to the grid independence

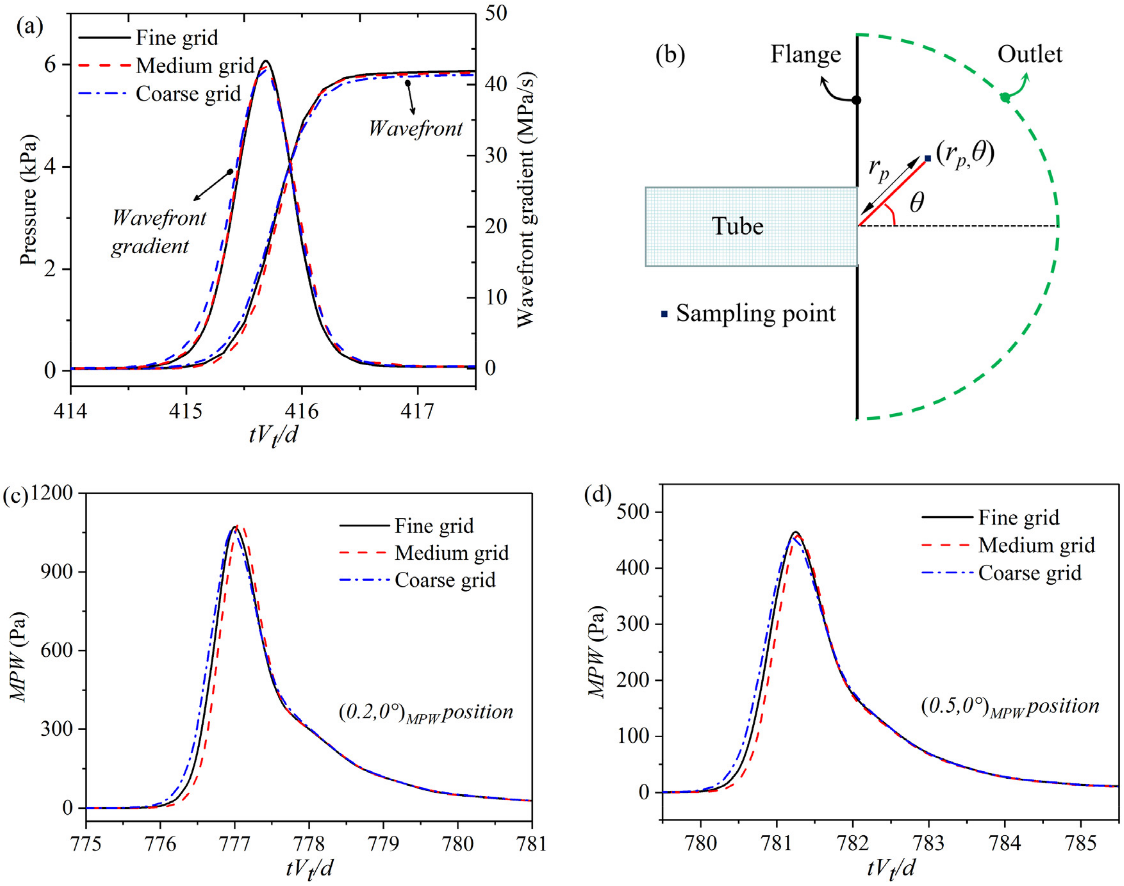

FIG. 4. Comparison of tube pressure and MPW data for three grid resolutions: (a) the temporal wavefront and the wavefront gradient at $x/L_{tu} = 0.5$ tube wall, (b) the definition of the MPW sampling points, (c) the temporal MPW at the $(0.2, 0)_{MPW}$ location, and (d) the temporal MPW at the $(0.5, 0)_{MPW}$ location.

test. Three different train head designs were employed to investigate the adaptability of the computational train appearance.[37] As validations for the nonlinear steepening of the wavefront profile and the characteristics of the MPW, the simulation data were compared with scaled moving-model experiments with the holographic interference observation.[12] Moreover, further exploration has been conducted on the modifications of gasdynamic features inside a tube with a specific speed of 500 km/h at different Reynolds numbers.[33] Note that the validation of train shape adaptability and wavefront steepening is performed using a three-dimensional model. The prediction accuracy differences between the three-dimensional model and the two-dimensional axisymmetric model are only compared in the analysis of Reynolds number effects.

1. The adaptability of the train shape

First, the ability of the computational model to accurately capture the wavefront within the tube for diverse train nose is assessed. Based on the scaled model experiment conducted by Maeda *et al.*,[37] this investigation adopts three specific nose shapes that are consistent with the experimental model: conical, parabolic, and elliptical. All trains are represented as rotating bodies with different transitions from their streamlined regions to the cylindrical cars. Their detailed geometric dimensions and streamlined main profiles are depicted in Figs. 5(a) and 5(b). The diameter of the tube is 0.172 m, so the corresponding blockage ratio is 0.116. The train speed is assigned as 232 km/h. The computational domain and grid settings are visualized in Figs. 5(c) and 5(d). The total number of grids for ellipsoid, paraboloid, and circular cone cases are 2.25×10^6, 2.16×10^6, and 2.02×10^6, respectively. The other solution settings follow the principles outlined in Sec. II C.

Figure 6 presents the comparison between simulation and experimental data of the temporal wavefront in the tube with three train noses. The results show that the simulated wavefront obtained in this study agrees well with the simulation data of Uystepruyst *et al.*[2] in both trend and amplitude. Due to possible interference from factors such as the traction rope in the experiments, the running speed of the train might vary and could not be maintained constant, resulting in minor differences with the simulated wavefront. Overall, compared with the experimental results, the maximum pressure errors of the current simulation for ellipsoid, paraboloid, and circular cone cases are 1.9%, 3.2%, and 7.8%, respectively.

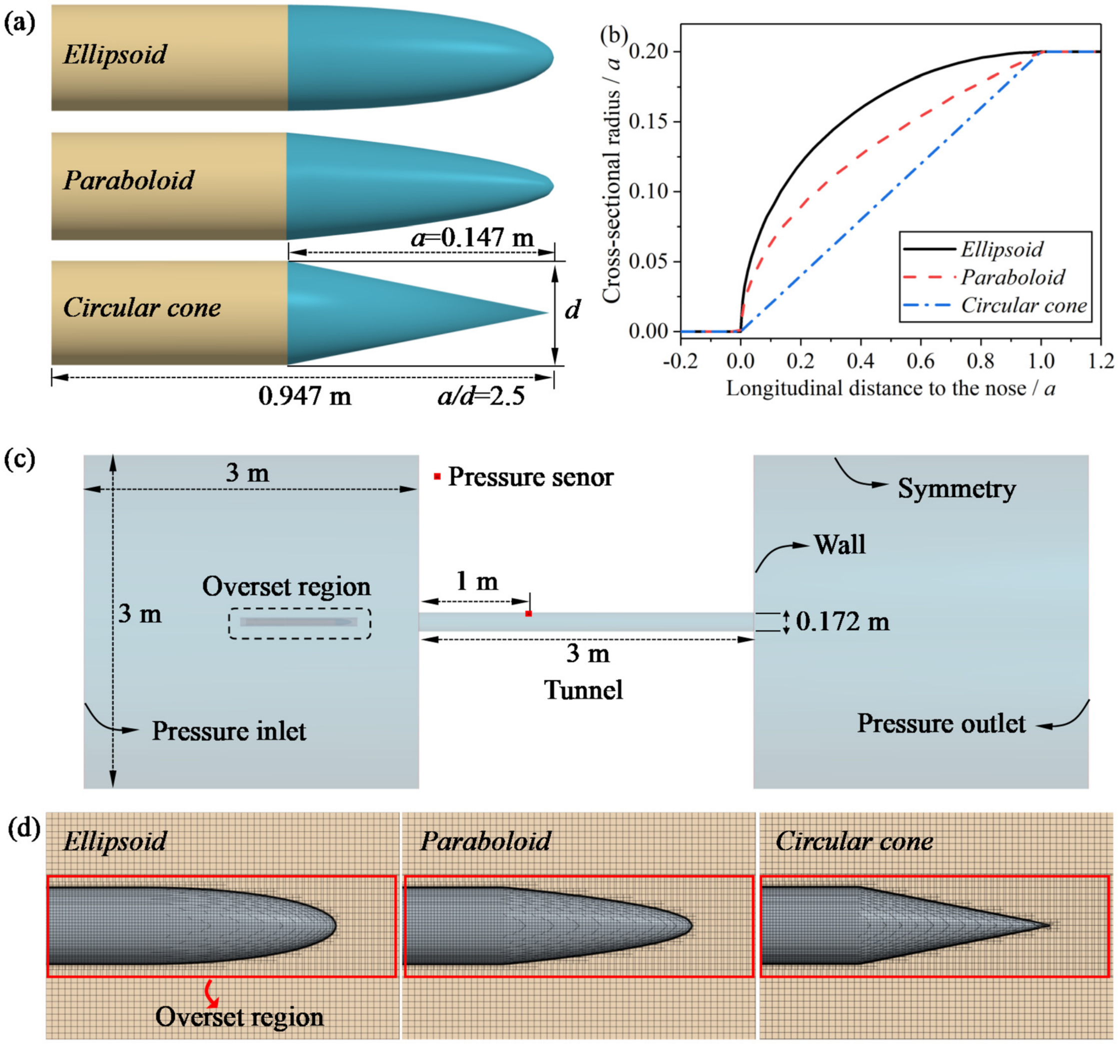

FIG. 5. Strategies for three-dimensional computing domains and grids of trains with different noses: (a) three train configurations, (b) the main profiles of the train nose, (c) computational domain and boundary conditions, and (d) grid strategies.

2. The comparison of steepening wavefront and MPW

The numerical setup to simulate the steepening wavefront, MPW and the formation of the WSW is validated by comparison with the experimental data obtained in a 1:300 scaled train/tunnel simulator at the Institute of Fluid Science, Tohoku University.[12] The piston was propelled by a launch tube, separated by a sabot separator, field into the test tube, and slid along the wall until it is braked by a piston stopper. The angle between the tunnel simulator and the ground was about 8, which allows the gravity acting on the piston to counteract the friction generated by the contact between the tube and the piston. The piston has a cylindrical shape with a diameter and length of 0.018 and 0.2 m, respectively. The diameter and length of the tube are 0.04 and 25 m, respectively, resulting in a corresponding blockage ratio of 0.2. Seven pressure transducers were distributed along the tube, starting from the inlet, and spaced 3.4 m apart, named PT1–PT7. Through a window installed at the tube end with dimensions of $0.03 \times 0.04 \times 0.25\ \mathrm{m}^3$, the holographic interferometry technique was employed to observe the WSW inside the tube. PT8 was installed at the middle of the window.

Figures 7(b) and 7(c) graphically portray the radiation processes of wavefront steepening and MPW excited by a 360 km/h piston within the tube. The velocity of the piston is inevitably attenuated during the experiment, leading to a slightly lower overall pressure in the experimental results than the simulation ones. However, the agreement between the two datasets regarding the shape of the wavefront distribution and its gradient is remarkable. Moreover, the wavefront gradient at PT5 location initiates a gradual increase, primarily due to the nonlinear steepening of the propagating compression wave, which is the root cause for the WSW formation. Turning to the MPW, there are two salient stages in its radiation process. The first one is the impulse wave generated by the propagating compression wave bursting

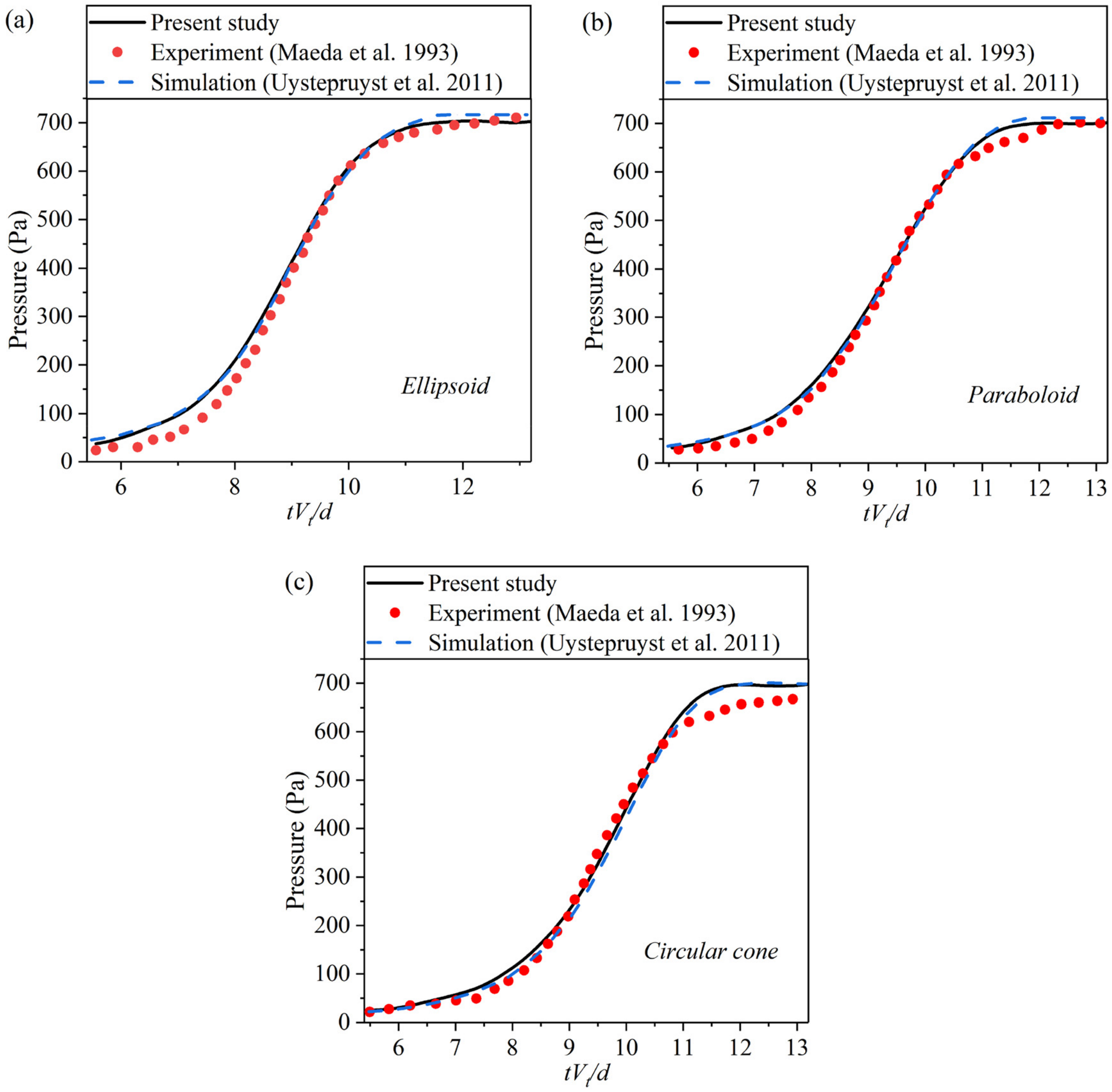

FIG. 6. Comparison of the temporal wavefront between the experimental and the simulation data for three train noses: (a) ellipsoid, (b) paraboloid, and (c) circular cone.

out of the tube. This MPW is no longer a simple symmetric pattern but assumes a triangular contour, reminiscent of the N-shape wave observed during an aircraft sonic boom. In this phase, the first peak in the experiment and simulation amount to 0.35 and 0.36 kPa, respectively. However, due to the enclosed experimental environment, a second peak appears upon reflection of the MPW. In contrast, the outlet boundary is treated as a pressure far-field in the simulation, which effectively rules out pressure reflection at the outlet boundary. Therefore, there is no observable second peak in the simulated data, rendering a more authentic representation of a real-world tunnel portal environment.

Therefore, understanding the formation of the WSW is an important factor in linking the results of wavefront steepening and the causes of sonic boom. The WSW generated with a 270 km/h has been comprehensively visualized and quantitatively analyzed in terms of the holographic interferometry, simulation schlieren, simulation shadowgraph, and simulation density [see Fig. 7(d)]. In the holographic interferogram, a noticeably abrupt transition occurs at the terminus of the tube. It can be ascertained that the propagating compression wave gradually coalesces into a WSW due to nonlinear steepening. In the current study, the simulation schlieren and simulation shadowgraph are implemented to observe changes in the first and second order differentials of gas density, enabling the visualization of shock waves. The instantaneous simulation schlieren (*ISS*) is plotted by the following equation, which is referring to the Wu's research:[38]

$$ISS = c_1 \exp\left[-c_2\left(|\nabla p| - |\nabla p|_{min}\right)/\left(|\nabla p|_{max} - |\nabla p|_{min}\right)\right], \qquad (1)$$

where the $|\nabla p|$ indicates the magnitude of wavefront gradient. The constants c_1 and c_2 are set to 0.8 and 1000, respectively, to reinforce the trend of density gradient variation in the flow field.

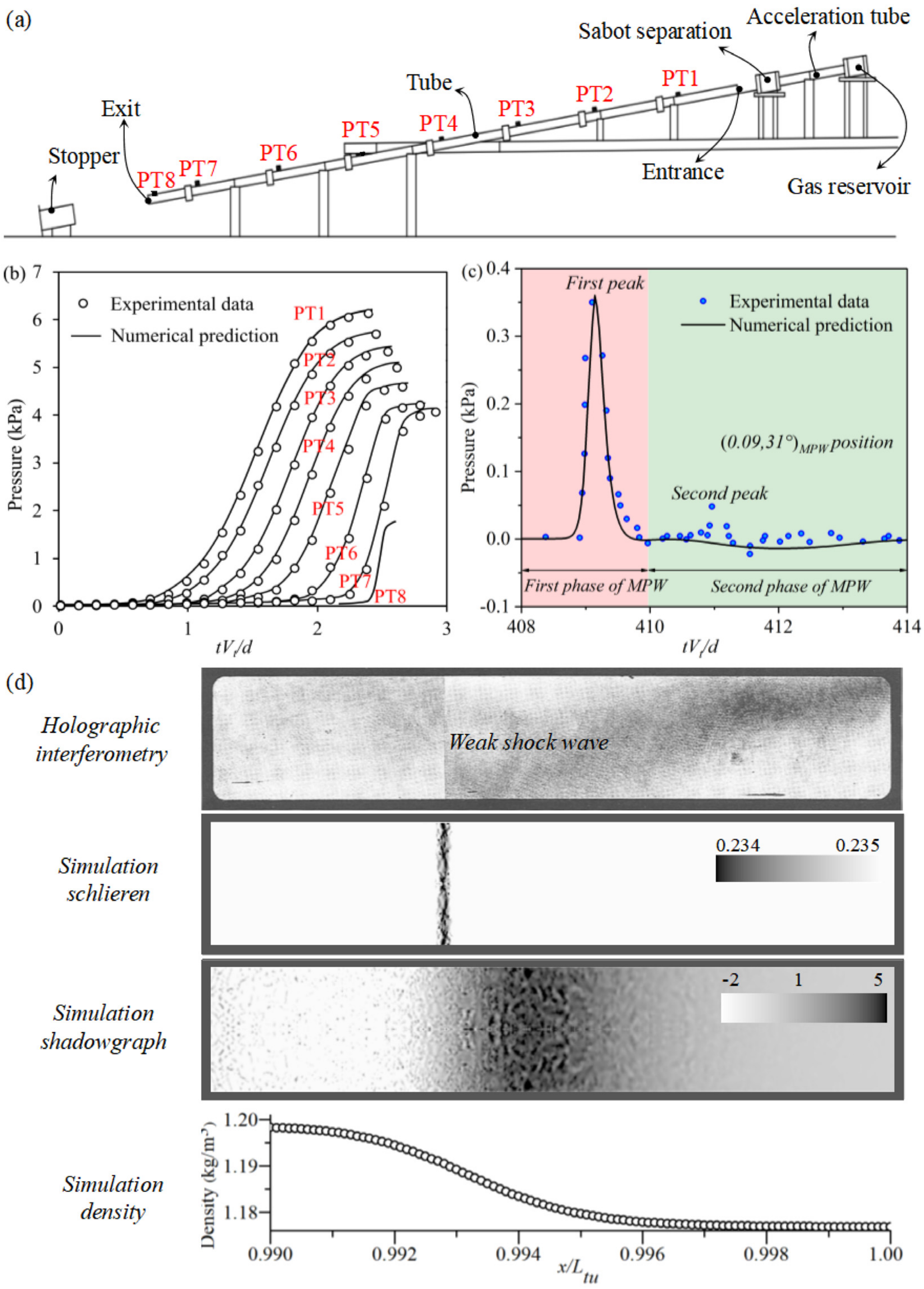

FIG. 7. The validation of the numerical simulations of steepening wavefront, MPW and the formation of the WSW: (a) a schematic of the 1:300 scaled train/tunnel simulator at the Institute of Fluid Science, Tohoku University,[12] (b) the comparison of the wavefront between the experimental data and the numerical prediction results, (c) the evolution of the radiated MPW at the $(0.09, 31)_{MPW}$ location, and (d) the formations of the WSW in terms of the holographic interferometry, simulation schlieren, simulation shadowgraph, and the simulation density. The angle between the tunnel and the floor is maintained at 8°. The piston speed in (b) and (c) is 360 km/h, and the piston speed in (d) is 270 km/h.

Simulation schlieren and simulation shadowgraph both confirmed the formation of the WSW presented in the experiment. For shock Mach number M_s approaching 1, the shock wave relationship can be simplified. According to the Rankine–Hugoniot relations for ideal gases with the specific heat ratio $\gamma = 1.4$, the shock Mach number can be evaluated using the positive overpressure Δp behind the planar shock wave by Eqs. (2) and (3).[10,39] Moreover, the density jump $\Delta\rho$ behind the planar shock wave can be evaluated by Eq. (5).[10] Here, p^* is the ambient atmosphere,

$$M_s = \sqrt{1 + \frac{\gamma + 1}{2\gamma}\frac{\Delta p}{p^*}}, \tag{2}$$

$$M_s^2 - 1 \cong 2(M_s - 1). \tag{3}$$

From Eqs. (2) and (3), we can derive[12]

$$\frac{\Delta p}{p^*} = \frac{4\gamma}{\gamma + 1}(M_s - 1), \tag{4}$$

$$\frac{\Delta\rho}{\rho} = \frac{4\gamma}{\gamma + 1}(M_s - 1). \tag{5}$$

The experimental and simulated overpressure at the piston speed of 270 km/h are 1.80 and 1.82 kPa (shown as the temporal wavefront of PT8), respectively. The corresponding experimental and simulated shock Mach numbers are 1.0076 and 1.0077, respectively. Through simulated density statistics within the WSW range, the local $\Delta p/p^*$ caused by the WSW is approximately 1.8%, which is 1.5% observed in the experiment. The $\Delta\rho/\rho$ estimated by Eq. (5) is 1.8%. Overall, the characteristics of wavefront steepening, WSW, density jump, and MPW in the simulation have been well validated by the experimental data.

3. The effect of Reynolds number

The previous verification investigation only covered train speeds up to 360 km/h and was calculated using a three-dimensional scaled model. However, current computational resources struggle to accommodate three-dimensional model calculations for long tunnels, and the influence of Reynolds number is still unclear. Therefore, the aim of this section is to validate the effectiveness of a two-dimensional axisymmetric model at 500 km/h and to investigate the influence of Reynolds number. The scaled dynamic model experimental facility of RTRI was described in Sec. II A, which mainly consists of a launcher, a braking device, and a tensioning device, with steel wires passing through the train model and fixed by the tensioning device. The experimental facility can ensure that the speed of the train from the launcher to the braking device is reduced by less than 1%. The parameters of the train and tunnel all referred to those mentioned in Table I (Sec. II A), with the exception that the tunnel length is $L_{tu} = 424.86d$, the streamline length is $L_l = 1.5d$, and the train speed is $V_t = 500$ km/h. More detailed geometric parameters for the experiments could refer to the research by Saito *et al.*[33]

As presented in Fig. 8(a), the temporal pressures at $x/L_{tu} = 0.16$ location for three methods are plotted. Both the numerical simulation of the three-dimensional model and the two-dimensional axisymmetric model have accurately predicted the data measured in experiments. Compared to the maximum positive pressure obtained experimentally, the differences of the numerical predictions by the three-dimensional model and the two-dimensional axisymmetric model are 1.4% and 4.9%, respectively. Additionally, the CPU solution time for the three-dimensional model and the two-dimensional axisymmetric model are the 51 862 and 1584 h, respectively. Compared to the three-dimensional model, the use of the two-dimensional axisymmetric model can reduce computational costs by nearly 96.9%. Therefore, the two-dimensional axisymmetric model can significantly reduce computational resources while maintaining prediction accuracy. Figure 8(b) illustrates the influence of the Reynold number on the wave effects inside the maglev tube. The range of Reynolds numbers selected is from 3.0×10^5 to 3.0×10^7, representing four typical scaling ratios of 1:97, 1:50, 1:25, and 1:1. As the Reynolds number increases, the maximum positive pressure shows a negligibly decreasing trend, but its wavefront gradient exhibits good consistency. The maximum positive pressure difference among the four Reynolds numbers is 4.5%. The Reynolds number independence is achieved for Reynolds numbers

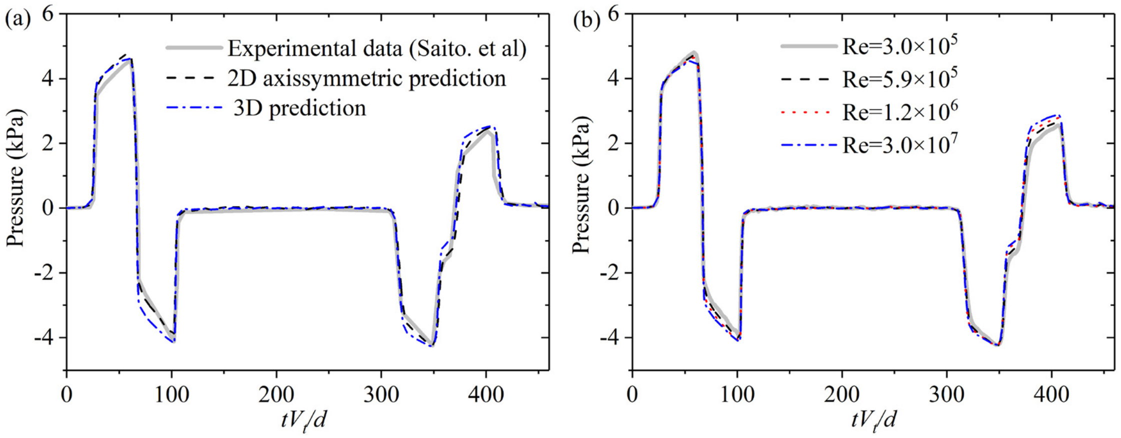

FIG. 8. The validation of the 2D axisymmetric model and the effect of the Reynold numbers: (a) the temporal pressure at $x/L_{tu} = 0.16$ location for three methods and (b) the temporal pressure at $x/L_{tu} = 0.16$ location for four different Reynold numbers.

above 3.0×10^5. Also, the adopting a two-dimensional axisymmetric model in the current study with a scaling ratio of 1:97 for solution is justified.

III. RESULTS AND DISCUSSION

A. Generation mechanism and characteristics of weak shock wave

1. The evolution characteristics of the wavefront

Sonic boom is generated by the radiation of WSW emanating from the exit of a tube. As the train speed of the current study completely falls within the subsonic range, the train will not generate WSW during its initial entry into the tube. In a linear theory, pressure disturbances propagate at a constant speed, which is equal to the sound speed C_0, and their fundamental mode is non-dispersive. However, the pressure disturbance propagates at a higher speed than C_0 as the magnitude of the pressure disturbance increases. The propagation velocity of the initial propagating simple wave is usually deviated from the speed of sound by $(\gamma + 1)u/2$, where u represents the particle velocity of the air.[10] The local overpressure $\Delta p \approx \rho C_0 u$ is almost proportional to the u. Although the deviation in propagation velocity from the speed of sound is small, the pressure profile of the initial compression wave progressively distorts under the action of local overpressure due to the large-length of the tube. Consequently, the initial wavefront experiences a nonlinear steepening and ultimately forms a pressure discontinuity known as the shock wave.[13,14] This represents the process of shock wave formation, which is also the primary objects in this article. As this shock wave is much smaller than those discussed in general gas dynamics, it is referred to the WSW.

Before delving into the physical process of WSW formation, it is appropriate to consider the pressure field generated by the train entering the tube. The current blockage ratio β of the maglev tube is 0.12, with train speeds ranging from 0.37M to 0.57M. One feature of tunnel structure is its very large ratio of length to hydraulic diameter. In this case, the length of tunnel where traditional a high-speed rail produces a sonic boom is typically around 8 km.[5] The distance of the WSW formation will be significantly shorter than 8 km at a higher train speed. Figure 9 presents the waterfall processes of the temporal pressure traveling along the maglev tube under the 450, 600, and 700 km/h train speed. From the perspective of wave propagation, the tube is a waveguide where pressure disturbances can freely propagate without any geometric diffusion. When the maglev train rushes into the tube, it replaces the air in the tube entrance area. Some of the air is expelled from the tube entrance to the external atmospheric environment, and the temporal pressure fluctuation at this location is relatively small. The other part is pushed forward into the tube interior, causing local disturbance of the air. This pressure disturbance, also known as the initial propagating compression wave, propagates forward along the tube at a speed of sound. Due to the slightly higher propagation speed of the wave in the pressurized area than the speed of sound, the temporal wavefront undergoes a nonlinear steepening phenomenon. In other words, the temporal wavefront gradually changes from a Gaussian-shaped waveform to a triangular waveform along the maglev tube, which can be clearly observed in Fig. 9(c). This phenomenon is very similar to the transition of near-field bow waves to far-field N-shaped waves in the aircraft sonic boom.[40]

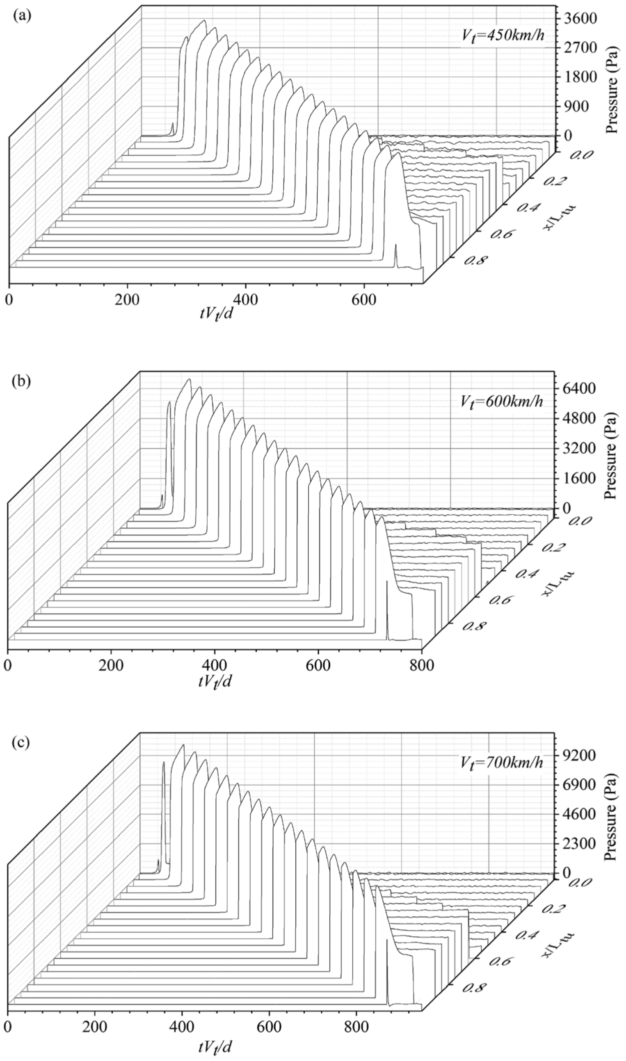

FIG. 9. The waterfall processes of the temporal pressure traveling along the maglev tube under the train speeds of: (a) 450, (b) 600, and (c) 700 km/h.

Therefore, the wavefront amplitude and the wavefront gradient amplitude along the tube need to be quantitatively analyzed. Figure 10(a) shows the wavefront amplitude along the tube for different train speeds. Due to the friction effect of the tube wall, the wavefront amplitude decreases to varying degrees. At the tube end, which is connected to the environment, the wavefront amplitude is relatively small. For a uniform tube with a hydraulic diameter of D, the wavefront thickness is of order DC_0/V_t.[41] The current research focuses on the influence of initial wavefront on sonic boom, so the wavefront characteristics at $x = DC_0/V_t$ location are used to evaluate the initial excitation in the tube. Figure 10(b) summarizes the initial wavefront at $x = DC_0/V_t$ location under different speed grades. The wavefront amplitude gradually increases with the increasing speed, while the wavefront thickness decreases accordingly. The comparison between the simulated amplitudes of the initial wavefront and the predicted values by Rivero *et al.*[13] [shown in Eq. (6)] is illustrated in Fig. 10(c). The prediction accuracy of empirical Eq. (6) has been well verified in numerous literature works.[13,42] In the current

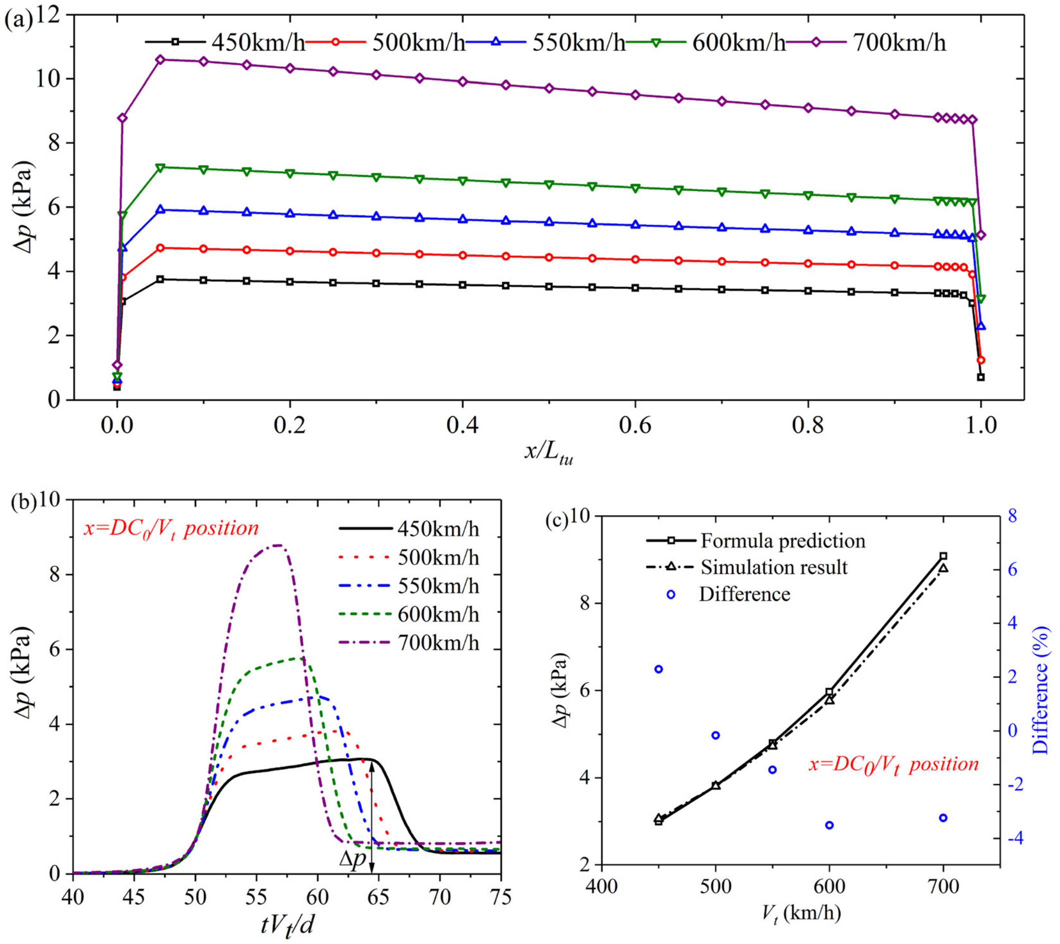

FIG. 10. The wavefront amplitudes and waveforms along the maglev tube at different train speeds: (a) the distributions of the wavefront amplitude, (b) the temporal initial wavefronts, and (c) the comparison of the initial wavefront amplitudes between the formula prediction and the simulation results.

calculation, the difference between the simulation results and the formula prediction values is within 3.6%,

$$\Delta p=\frac{1}{2}\gamma p^{*}M^{2}\frac{1-(1-\beta)^{2}}{(1-\beta)^{2}+\left(1-(1-\beta)^{2}\right)M-M^{2}},\tag{6}$$

$$\xi=\frac{\left[\frac{dp}{dt}\right]_{max}(x)}{\left[\frac{dp}{dt}\right]_{max}\left(x=\frac{DC_0}{V_t}\right)},\tag{7}$$

$$\left[\frac{dp}{dt}\right]_{max}\left(x=\frac{DC_0}{V_t}\right)=0.4\frac{\Delta pV_t}{L_1}.\tag{8}$$

The distributions of the wavefront gradient amplitude along the tube at different speeds are shown in Fig. 11(a). When the streamlined head train enters the tube, an initial wavefront excitation is formed. After that, the wavefront profile becomes steeper under the driving of nonlinear steeping, that is, the wavefront gradient amplitude gradually increases. When the initial propagating compression wave coalesces into a WSW, the wavefront gradient amplitude reaches its maximum value. After the formation of the WSW, the wavefront gradient amplitude only exhibits small fluctuations. The wavefront gradient amplitude generated by subsequent nonlinear steeping is less than that at the location of the WSW. The distance between the location of the tube inlet and the maximum wavefront gradient amplitude is defined as the formation distance of the WSW (L_s). To facilitate comparison with the actual tunnel length where the sonic boom occurs, the L_s in the current study is the full-scale length. The L_s at speeds of 450, 500, 550, 600, and 700 km/h are 2.75, 2, 1.5, 1.25, and 0.75 km, respectively. In other words, when the blockage ratio is 0.12 and the length of the maglev tunnel exceeds 1.25 km at $V_t = 600$ km/h, a WSW will form and propagate to the tunnel exit. Eventually, the WSW will radiate into the surrounding environment, causing unpleasant sonic booms or vibration of the surrounding building door/window frames. Additionally, the nondimensional distortion rate ξ is defined by Eq. (7), with the wavefront gradient amplitude at $x = DC_0/V_t$ as the reference. Figure 11(b) shows the nondimensional distortion rate of the wavefront gradient amplitude

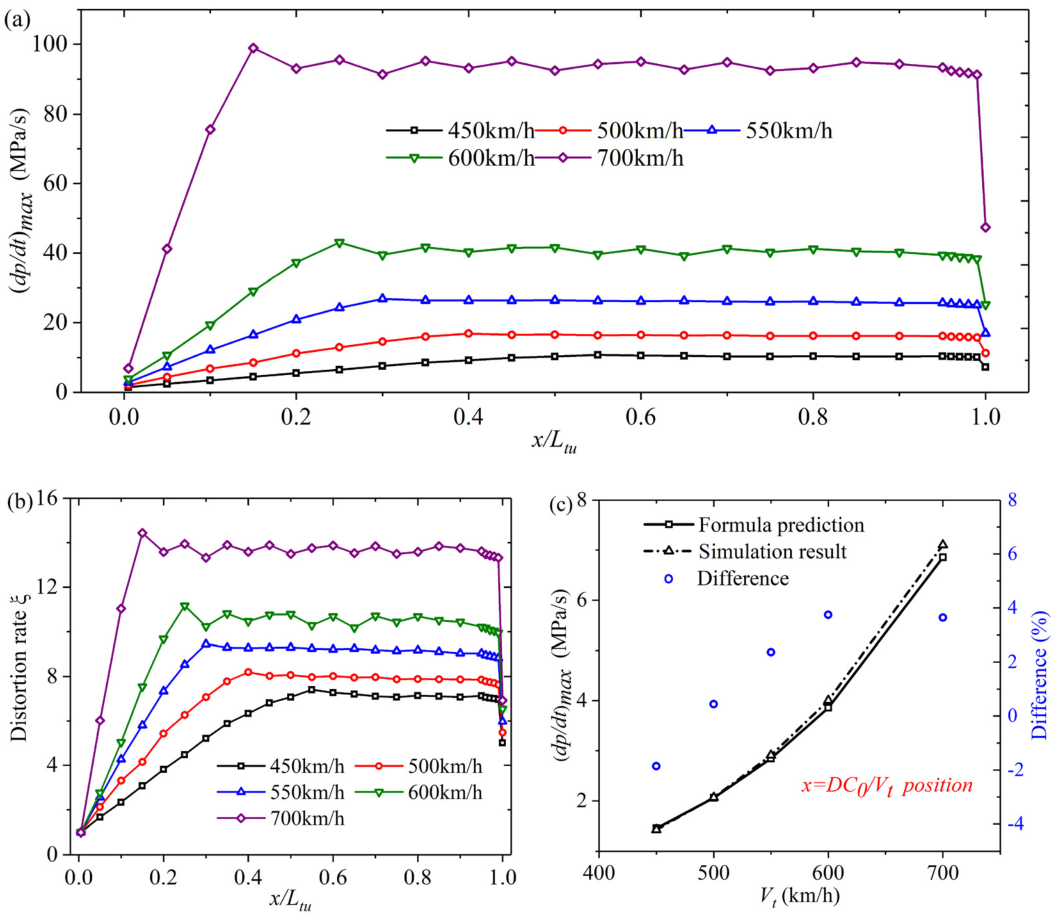

FIG. 11. The wavefront gradient amplitude along the maglev tube: (a) the distribution of the wavefront gradient, (b) the evolution of the nondimensional distortion rate ξ, and (c) the comparison of the initial wavefront gradient between the formula prediction and the simulation results.

along the tube, which presents a clearer observation of the variation trend of the wavefront gradient amplitude than Fig. 11(a). The functional expression for the initial wavefront gradient amplitude is given in Eq. (8).[19] The prediction accuracy has been well validated in the Rivero *et al.*'s study.[13] The simulation results of the initial wavefront gradient amplitude are compared with the formula prediction in Fig. 11(c). The difference between the simulation results and the formula prediction values is within 3.9%.

2. The formation distance of the weak shock wave

The characteristics of the initial wavefront have been comprehensively analyzed by above simulated and theoretical results. In general, the scenario of a train running inside a tube is similar to a piston driven inside a shock tube, except that the train plays the role of a "leaky piston." According to the theory of one-dimensional unsteady compressible tube flow, the distance at which the initial compression wave transforms into a WSW can be evaluated from a theoretical analysis perspective. Equation (9) is the theoretical prediction of the full-scale formation distance of the WSW,[10] in which the amplitude of the initial wavefront gradient is based on Eq. (8),

$$L_s = \frac{2\gamma}{\gamma+1}\frac{p^* C_0}{\left[\dfrac{dp}{dt}\right]_{max}\left(x=\dfrac{DC_0}{V_t}\right)/97}. \tag{9}$$

After establishing the theoretical prediction of L_s, it is valuable to compare it with existing sonic boom incidents at the exit of railway tunnels. Combining the two parameters of blockage ratio (β) and train speed, Fig. 12 shows a comprehensive comparison of theoretical predictions of L_s with previous research,[14] sonic boom events,[4,5,43] and experimental result.[12] The speed ranges of high-speed trains and maglev trains are 200–450 and 450–700 km/h, respectively. The colored area overlaid the theoretical prediction on the upper-left corner represents the potential tunnel length for sonic boom occurrence. Wang *et al.*'s[14] research summarizes the L_s in the 200–350 km/h range with an unsteady friction coefficient of 0.01 and a steady friction factor of 1. Their L_s data are the closest to the theoretical prediction value in this article under the blockage ratio of $\beta = 0.11$. The magenta rectangle represents the statistics of the China Academy of Railway Sciences on the sonic boom phenomenon in current operational tunnels in China.[43] Among them, there is only one tunnel with a length of 4–6 km, 37 tunnels with a length of 6–8 km, 24 tunnels with a length

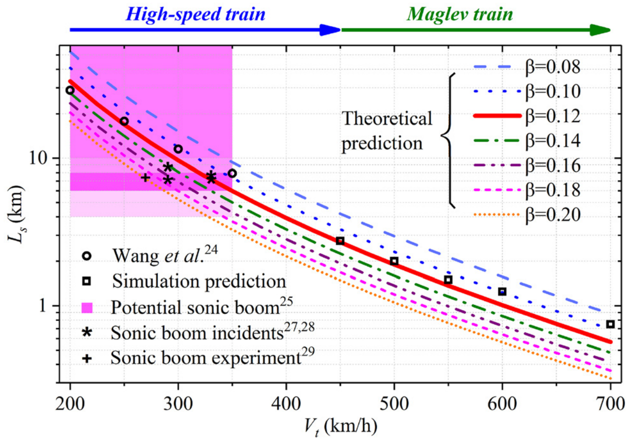

FIG. 12. The full-scale formation distance of WSW in a tube caused by the wavefront under different blocking ratios. The speed ranges of a high-speed train and a maglev train are 200–450 and 450–700 km/h, respectively. The theoretical predicted data are obtained in Eqs. (6)–(9).[10,13] The L_s for the speed range of 200–350 km/h is obtained from Wang *et al.*'s research.[14] The L_s predicted by simulation is determined by the maximum wavefront gradient in Fig. 11(b). The statistical graph of tunnel length for sonic boom phenomenon (potential sonic boom) in high-speed railway tunnels is taken from Wang *et al.*'s study.[43] The probability of sonic boom occurrence is represented by the color intensity, with deeper colors indicating higher probabilities. The sonic boom records of the Irahull, Euerwang, La Cabrera, and San Pedro tunnels are taken from the investigations of Gerbig *et al.*[4] and Silvia *et al.*.[5] The $L_s = 7.45$ km measured by the sonic boom experiment[12] is consistent with Fig. 7. For specific data, refer to the main text.

of 8–10 km, and 29 tunnels with a length of more than 10 km. This rectangular box well covers the potential sonic boom tunnel length predicted by Eq. (9). Moreover, the detailed parameters of the tunnels and trains in the four sonic boom incidents are listed in Table III.[4,5] In the actual tunnel, the ballast form, shape of the tunnel portal, ventilation shaft, etc., are different from the simulation model. Additionally, the head shape and the cross-sectional area of the train also have a significant impact on the initial wavefront gradient. Hence, the length of these four tunnels is either greater than or close to the theoretical L_s. The ideal data would be experimental data from the train/tunnel simulator.[12] In the case of $V_t = 270$ km/h and $\beta = 0.20$, the experimental and theoretical L_s are 7.45 and 7.23 km, respectively, with a difference of only 3.0%. Additionally, the simulation L_s results for the 450–700 km/h range are also plotted. Overall, the theoretical formulas above achieve good L_s prediction of data obtained from sonic boom incidents, experiments, and simulations.

TABLE III. Statistics of key parameters of the tunnels where sonic boom occurs.

Cases	V_t (km/h)	L_{tu} (km)	β	Theory, L_s (km)
Irahull tunnel[4,5]	330	7.26	0.11	7.93
Euerwang tunnel[4,5]	330	7.70	0.11	7.93
La Cabrera tunnel[5]	289	7.25	0.18	6.70
San Pedro tunnel[5]	289	8.70	0.18	6.70
Experimental tunnel[12]	270	7.50	0.20	7.23

Based on the L_s obtained from Fig. 11, the simulated shadowgraph and the density distribution near the WSW are displayed in Fig. 13. From a physical perspective, a weak shock wave has a finite and measurable thickness, while the thickness of a strong gas shock wave is roughly equivalent to a few molecular mean free paths. The shock thickness reflects the relaxation process of transition from one equilibrium state of the fluid particles to another, and the internal structure of the shock wave is a highly complex problem that is closely related to internal viscosity and thermal conduction. Typically, a shock wave of certain strength is considered as a discontinuous jump surface, and the focus is on the relationship between the changes in parameters on both sides of the shock wave. However, in this study, the shock wave has a M_s between 1.015 and 1.045, making it a very weak shock wave (WSW). Therefore, the continuous transition length of this WSW is relatively large. As shown in the shadowgraph of Fig. 13, the compressive wave appears to coalesce into a WSW at the position L_s. Due to the density curve gradually approaching two limiting values upstream and downstream of the WSW, we define the WSW thickness δ as the horizontal distance between the two intersection points of the straight line passing through the inflection point of the density profile and the two limiting density lines. Therefore, the corresponding parameters of overpressure amplitude, shock Mach number, density jump, and WSW thickness are presented in Fig. 14. The overpressure amplitude, shock Mach number, and density jump all increase with the increasing train speed, while the WSW thickness decreases. Summarily, the quantitative analysis of the formation distance of WSW and the physical parameters near them have been completed. Hereinafter, this study will focus on the sonic boom phenomenon caused by the release of the WSW from the tunnel exit.

B. Spatial distribution and spectral characteristics of MPW

The sound pressure level (*SPL*) of the sonic boom is related to the MPW magnitude, and is usually proportional to the exit wavefront gradient.[6] The relationship between the wavefront exits gradient and the train speed is fitted from the data in Fig. 11(a) and presented in Eq. (10). The exit wavefront gradient is proportional to the 4.39th power of the train speed, which differs from the typical cubic relationship.[9] The main reason for the difference is the nonlinear steepening effect of the propagating compressional wave, as previously analyzed. The MPW magnitude, Δp_{MPW}, can be evaluated using Eq. (11).[23] Where S is the cross-sectional area of the tube, the radiation solid angle, Ω, of the circular tube is 2π, and $(dp/dt)_{exit}$ represents the exit wavefront gradient. The comparison between the simulated and formula-predicted Δp_{MPW} at the $(0.2, 0)_{MPW}$ location is illustrated in Fig. 15(d), and the difference between them is within 3.2%. Therefore, the MPW magnitude of the maglev tube can be well predicted by Eq. (11),

$$\left[\frac{dp}{dt}\right]_{exit} = 2 \times 10^{-10} V_t^{4.39}, \tag{10}$$

$$\Delta p_{MPW} = \frac{2S}{\Omega r_p C_0}\left[\frac{dp}{dt}\right]_{exit} = \frac{2S}{2\pi r_p C_0}\left[\frac{dp}{dt}\right]_{exit} = \frac{R^2}{r_p C_0}\left[\frac{dp}{dt}\right]_{exit} = \frac{2 \times 10^{-10} R^2 V_t^{4.39}}{r_p C_0}. \tag{11}$$

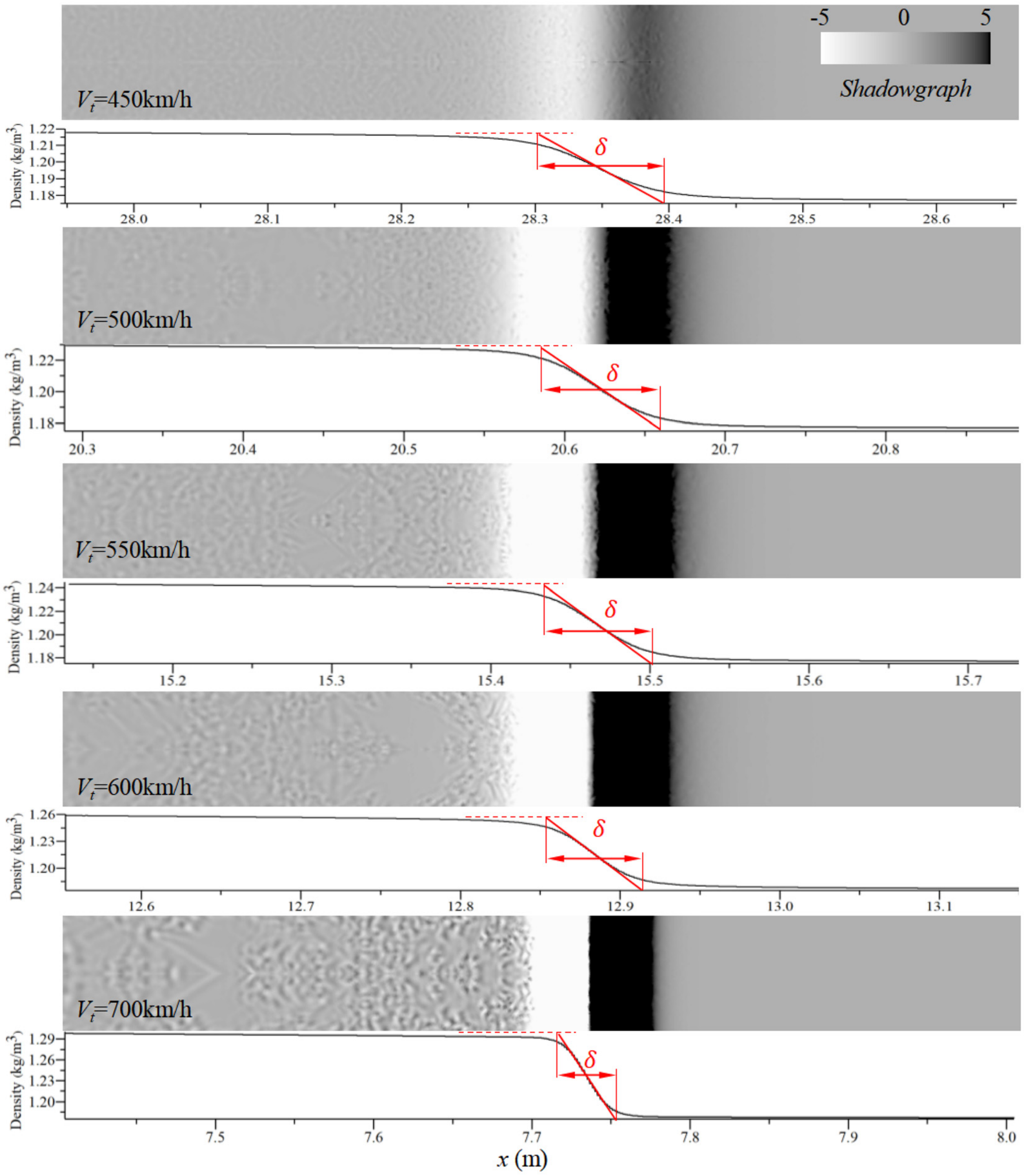

FIG. 13. The WSW shadowgraph in the maglev tube and density jumps behind the WSW at different train speeds.

The MPW characteristics along the axial direction at train speed of 450 and 600 km/h are presented in Figs. 15(a) and 15(b), respectively. Figure 15(c) displays the axial distribution of MPW amplitude for all speed grades. A short-duration impulse is excited by the WSW mentioned earlier, with a duration of only 1.7×10^{-3} to 2.6×10^{-3} s. Although the wavefront gradient amplitude at the outlet position has been significantly reduced relative to its maximum values [as shown in Fig. 11(b)], the MPW amplitude exceeds the existing standards for all speed grades.[11] In the case of a sonic boom caused by an aircraft, as a reference, the pressure rise caused by the N-shaped wave is generally $10^{-3}\,p^*$, with a rise time of 10^{-4}–10^{-2} s.[44] The large impulse amplitude (even as high as $3.4 \times 10^{-2}\,p^*$ at $V_t = 700$ km/h) that occurs at the tube exit in a short period of time ultimately leads to a sonic boom which is like that happened to an aircraft. As shown in Eq. (11), the MPW amplitude is inversely proportional to r_p and decreases along the axial direction consequently. Additionally, it is interesting to note that the MPW shape remains a Gaussian-shape at $V_t = 450$ km/h. However, there is a transition from a triangular waveform to a Gaussian-shape waveform at $V_t = 600$ km/h. This transition is related to the energy dissipation of the impulse wave, where the triangular waveform gradually flattens during propagation.

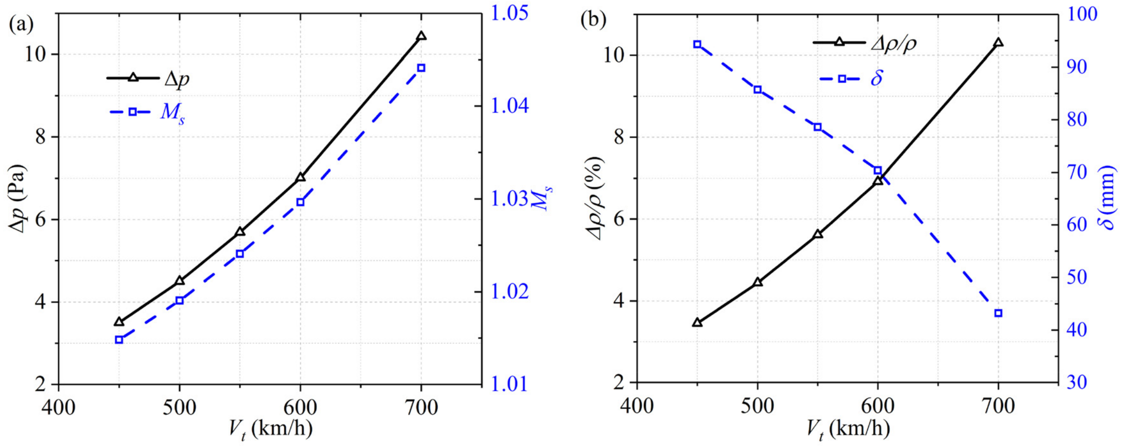

FIG. 14. Changes in physical quantities behind a WSW at different train speeds: (a) the pressure jumps behind the WSW and the shock Mach numbers and (b) the density jumps behind the WSW and the WSW thickness.

Figure 16 shows that the magnitude of MPW has a significant directional dependence. The magnitude of MPW in the axial direction is the largest at the same radius, while the magnitude of MPW perpendicular to the axial direction is significantly reduced, and this phenomenon is further enhanced with increasing speed (as shown in Fig. 17). However, as MPW propagates downstream, the difference in the MPW magnitude in the axial and perpendicular directions at the same radius decrease. This directional dependence of MPW has also been confirmed in many literatures.[3,14,23,45] A reasonable explanation is the influence of wavefront thickness. According to the data in Fig. 14(b), as the speed increases, the wavefront thickness decreases while the wavefront frequency increases. The directivity of MPW amplitude will increase with a higher wavefront frequency.[25] Therefore, the directivity of MPW amplitude will become more significant with the increase in train speed. Another explanation is related to the evolution process of the radiation of the impulse wave. As shown in Fig. 18, the impulse wave exhibits an elliptical state rather than a spherical state in the initial stage. Therefore, most of the energy is concentrated in the axial direction, resulting in a larger MPW amplitude in the axial direction, while the impulse energy perpendicular to the axis is less. In previous studies, scholars simulated relatively short time of the impulse wave.[3,45] In the current study, another interesting finding is that the semi-ellipsoid shape gradually transforms into a semi-sphere as the impulse wave propagates forward. This is also the reason why the directional dependence of the MPW amplitude weakens as the impulse wave propagates downstream.

The spectral characteristics and selection principles of MPW are illustrated in Fig. 19. The sound pressure level (SPL) is defined by Eq. (12), where p represents the measured sound pressure, p_r represents the reference sound pressure, usually taken as 2×10^{-5} Pa. As illustrated in Fig. 19(a), [T_0, T_1], [T_1, T_2], and [T_0, T_2] represent the first stage of the MPW radiation, the second stage of vortex ring influence, and the whole stage of the MPW radiation, respectively. The first peak is generated by the impulse wave in the first stage, while the second and third peaks are generated by the vortex rings that falloff at the connection between the tube and the flange. Figure 19(b) shows the spectral distribution of MPW in the intervals [T_0, T_1] and [T_0, T_2]. The data show that the SPL of MPW is greatly affected by the selected time interval. Generally, the interval [T_0, T_1] should be utilized as the data source for analyzing the spectral characteristics of MPW. MPW generally exhibits a low-frequency state, and most of the energy is concentrated in the infrasonic range. Therefore, in addition to the commonly used A-weighted method for acoustic analysis, C-weighted results are used to enhance the SPL in the low-frequency range. Figure 19(c) shows that the difference between A-weighted and C-weighted SPL is not significant. However, they have significantly lower SPL than the unweighted SPL in the frequency range above 100 Hz. Therefore, unweighted SPL is used to evaluate the equal-loudness-level of the human ear, while C-weighted SPL is used for comparison with European directive 2003/10/EC[27]

$$L_p = 20lg\frac{p}{p_r}. \tag{12}$$

Figure 20 presents the equal-loudness-level contours at the $(0.2, 0)_{MPW}$ position and the $(0.5, 0)_{MPW}$ position. The human ear structure determines that the loudness of a sound is largely based on its intensity and spectrum. When it comes to sounds like pure tones or narrowband noise, the equal-loudness-level can be defined as a measure of the sound's loudness at different frequencies. This concept is commonly used to reveal the frequency-dependent characteristics of our auditory system.[28] The equal-loudness-level shown in Fig. 20 brings up a few noteworthy points. Initially, due to the absence of experimental data at high loudness levels, the 100 Phon contour extends up to 1 kHz. Second, only equal-loudness-levels for 40, 70, and 100 Phon are mentioned. Finally, the hearing threshold and feeling threshold refer to the minimum sound level required for human ears to perceive a sound and to experience discomfort, respectively. Figure 20 illustrates that the lowest frequency of MPW's SPL increases as the speed increases. This is primarily attributed to the wavefront thickness mentioned earlier, whereby higher speeds result in reduced wavefront thickness and subsequently higher frequencies. Additionally, the SPL in the infrasound range of MPW surpasses the audible range SPL by a significant margin. MPW's SPLs at both positions depicted in Fig. 20 exceed the hearing threshold at all speed levels, generating substantial sonic

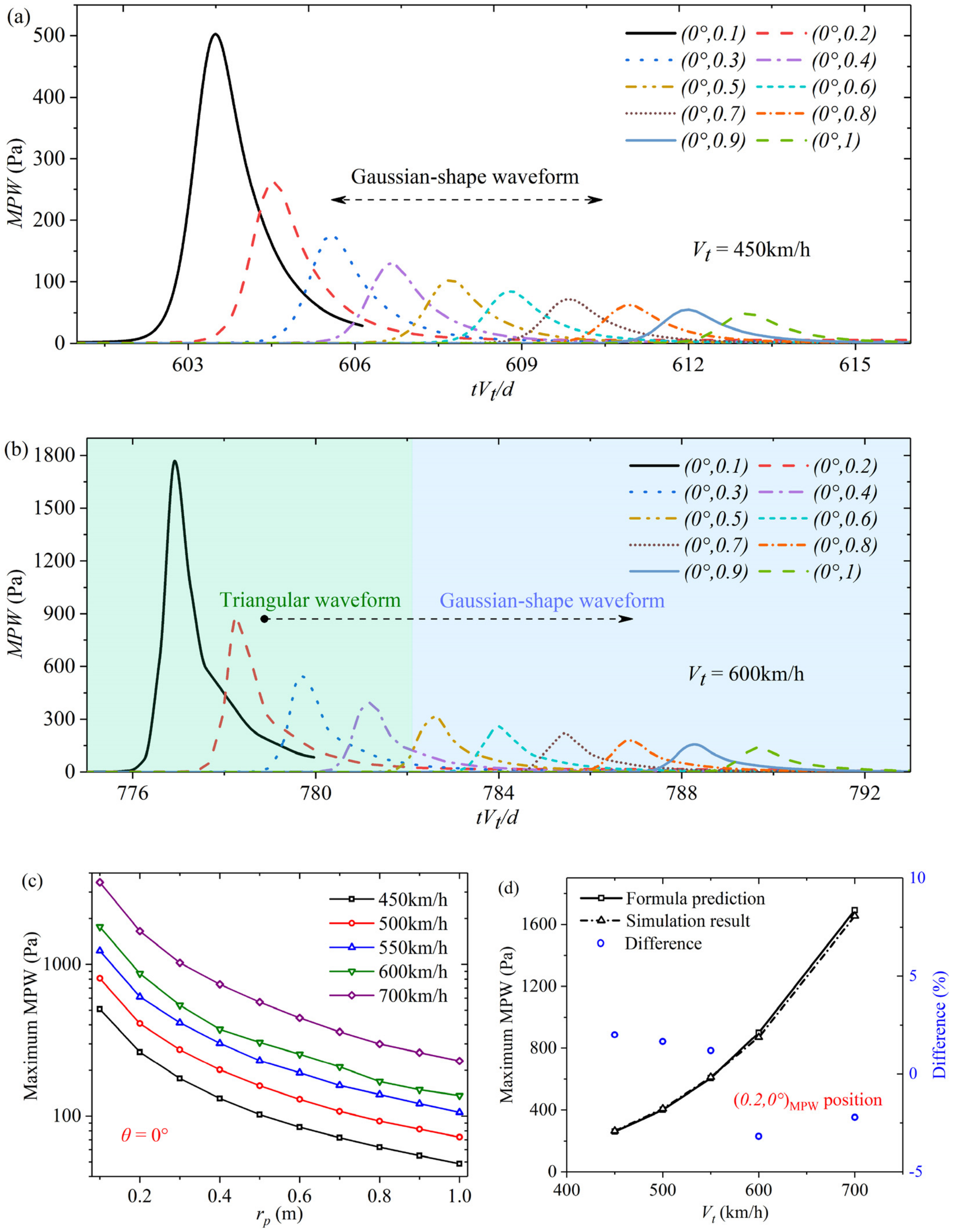

FIG. 15. The characteristics of the MPW: (a) temporal curves of the MPW along the streamwise direction at 450 km/h, (b) temporal curves of the MPW along the streamwise direction at 600 km/h, (c) The distribution of MPW amplitude along the streamwise direction at different train speeds, and (d) the comparison of the MPW amplitude between the formula prediction and the simulation results.

booms. When $V_t = 700$ km/h, the SPL at the $(0.2, 0)_{MPW}$ position even surpasses the feeling threshold within the 20–90 Hz range. As will be shown later, the SPL decreases with increasing propagation distance, and this attenuation trend is also summarized in Fig. 25(a).

C. Generation and evolution of vortex ring

The propagating wavefront first radiates a portion of its energy in the form of an impulse wave, and then generates vortex ring structures in the form of a jet flow [as shown in Figs. 19(a) and 21].

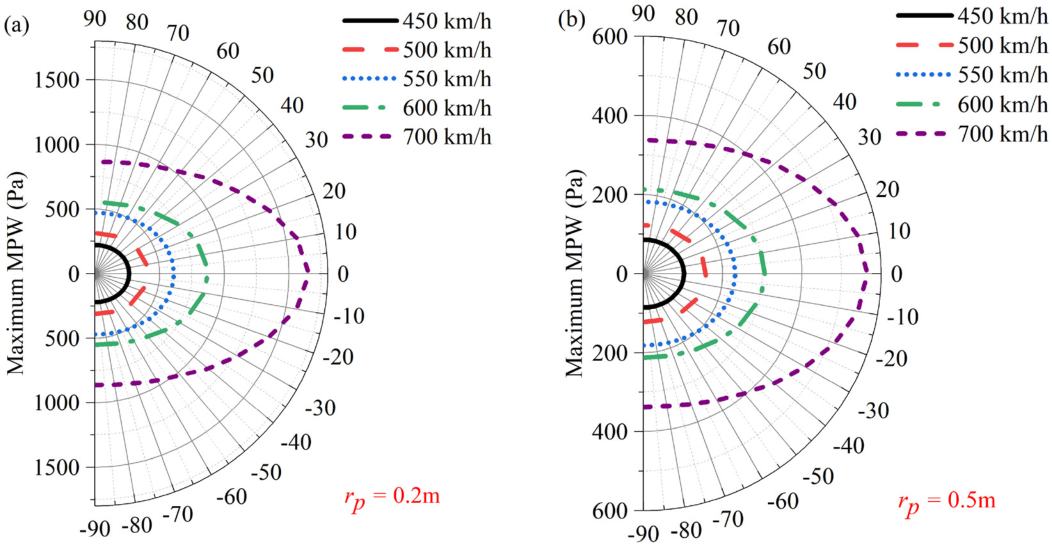

FIG. 16. The directivity of MPW amplitude in terms of different train speeds: (a) at the specified radius $r_p = 0.2$ m and (b) at the specified radius $r_p = 0.5$ m.

When $M_s < 1.43$, the CVR is typically a shock-free CVR.[29,31] The maximum M_s observed was 1.04 in the current study, and no shock structure was observed during the evolution of the vortex ring. Figure 21(b) demonstrates that the evolution of the CVR occurs in four stages: rapid growth stage, pinch-off stage, free development stage, and disappearance stage.[32] First, the primary compressible vortex ring (PCVR) (a pair of small vortex cores) is generated due to the large velocity gradient at the connection between the tube and the flange, and it wraps around the leading pressure waves. Then, the size of the PCVR grows rapidly and starts moving downstream along the axial direction once it reaches a certain size. In the shadowgraph at $tV_t/d = 829$, the trailing jet can be observed behind the PCVR, and they interact with each other. Due to the lack of vorticity between the PCVR and the trailing jet,[30,46,47] the PCVR is separated (also known as pinch-off) with the trailing jet and its free development downstream. Meanwhile, the secondary compressible vortex ring (SCVR), which is further away from the PCVR, is generated behind the PCVR. The shear layer of the trailing jet behind the SCVR forms a series of Kelvin–Helmholtz vortices (K-HV). The K-HV starts rotating and absorbs vorticity from the upstream and downstream of the shear layer vortices, resulting in continuous generation, merging, and downstream development of K-HV. In the free development stage, the vortex core of the PCVR continues to grow until the disappearance stage, and a vortex plane forms in front of the SCVR at $tV_t/d = 1151$. The MPW at the axial position in Fig. 21(b) is mainly influenced by the PCVR because its influence extends to the axial position. As presented in Fig. 21(a), the MPW data

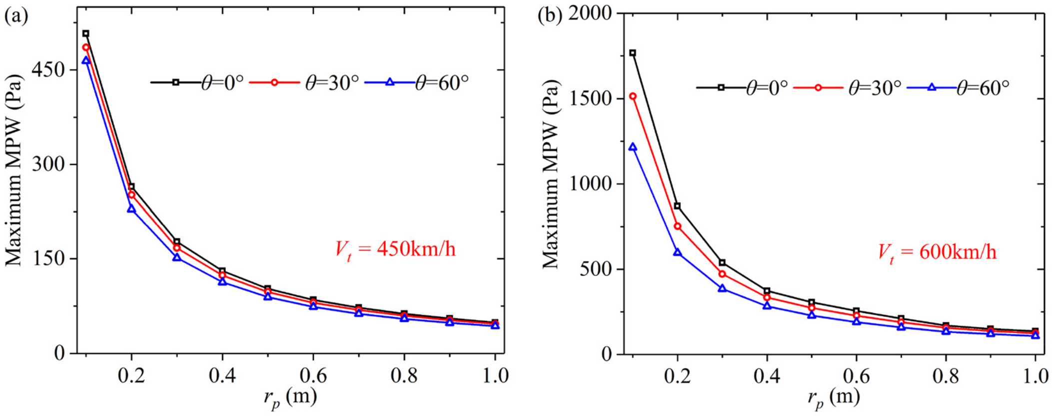

FIG. 17. The distribution of the MPW amplitude along the streamwise direction at different directivity angles: (a) a specific train speed of 450 km/h and (b) a specific train speed of 600 km/h.

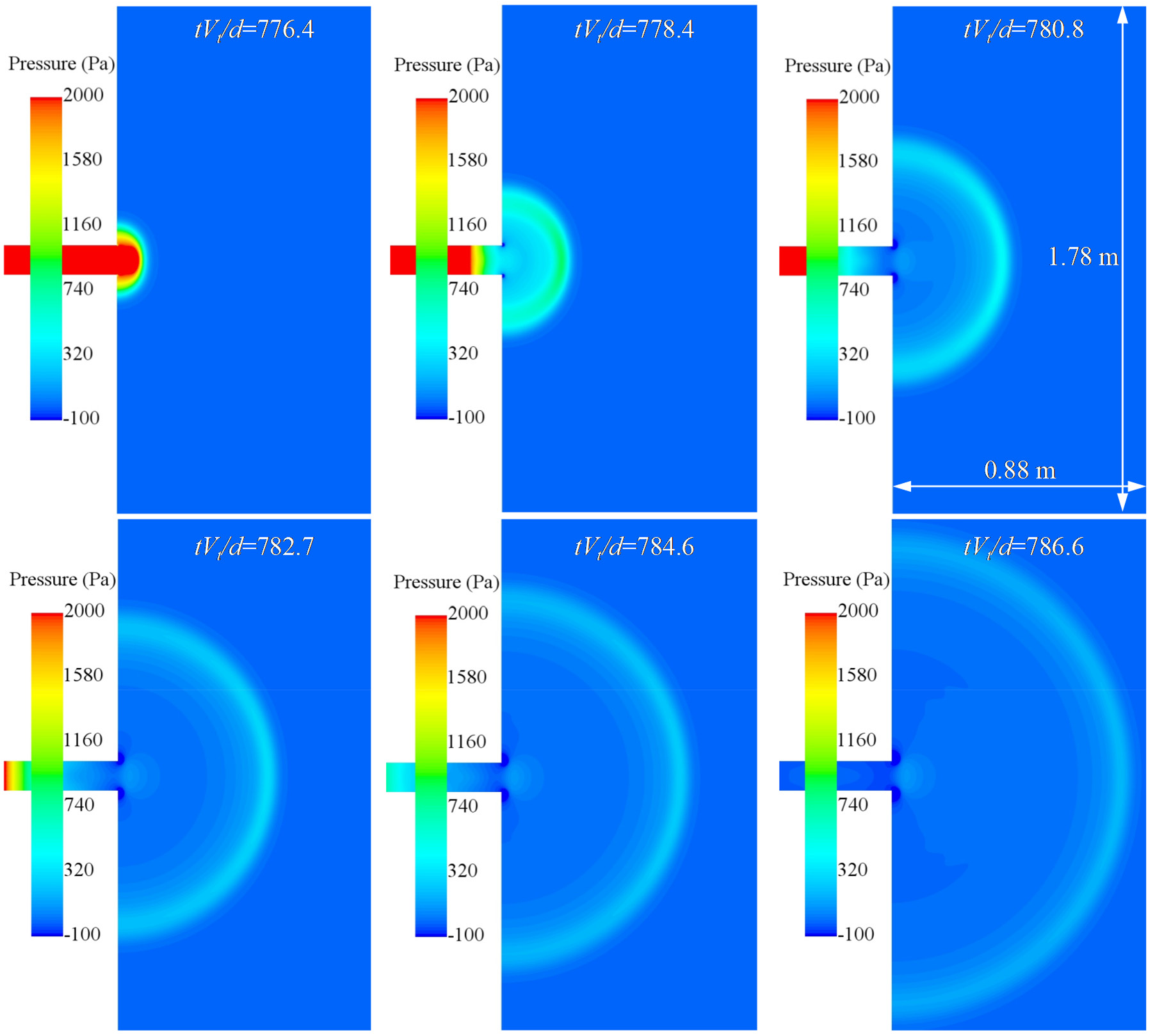

FIG. 18. Evolution process of MPW radiation at 600 km/h train speed.

at the $(0.2, 0)_{MPW}$ position indicate that the MPW rises and reaches the second peak when the PCVR reaches the measurement point. As the outer edge of the PCVR passes through the measurement point, the MPW decreases due to the increase in flow velocity.[48] When the trailing flow after pinch-off reaches the measurement point, the MPW rises again and reaches the third peak. Noted that the influence range of the vortex ring of the MPW is limited in the circumferential direction (within a cylinder with a diameter of 2.3D centered on the tube). Therefore, the discussion of the maglev tube extends the previous discussion of CVR in the railway tunnel and helps us to understand the reasons for the fluctuations in the later stage of the MPW.

The above analysis shows that PCVR has the greatest impact on the axial MPW. While $800< tV_t/d <1200$, the shadowgraph images of PCVR are automatically saved at a time step of 2.5×10^{-6} s. Based on the geometric characteristics of PCVR in shadowgraph images during this period, its kinematic and geometric properties are obtained. Therefore, Fig. 22 summarizes the evolution of PCVR translational velocity, displacement, ring diameter, core diameter, and the ratio of the ring diameter to the core diameter at $V_t = 600$ km/h. PCVR continued to move in an open space for about 0.7 m from its generation at 600 km/h train speed. As illustrated in Fig. 22(a), before the pinch-off process, the translational velocity of PCVR continued to increase and reached its maximum at $tV_t/d = 900$. However, due to the energy loss caused by the pinch-off process, the translational velocity of PCVR gradually decreased. Meanwhile, the ring diameter of PCVR rapidly increased during the rapid growth stage [as shown in Fig. 22(b)]. After that, PCVR basically moved downstream along the axis, and its ring diameter grew slowly. However, PCVR expanded quickly in the radial direction after the pinch-off process. During the disappearance stage of PCVR, its ring diameter gradually decreased.

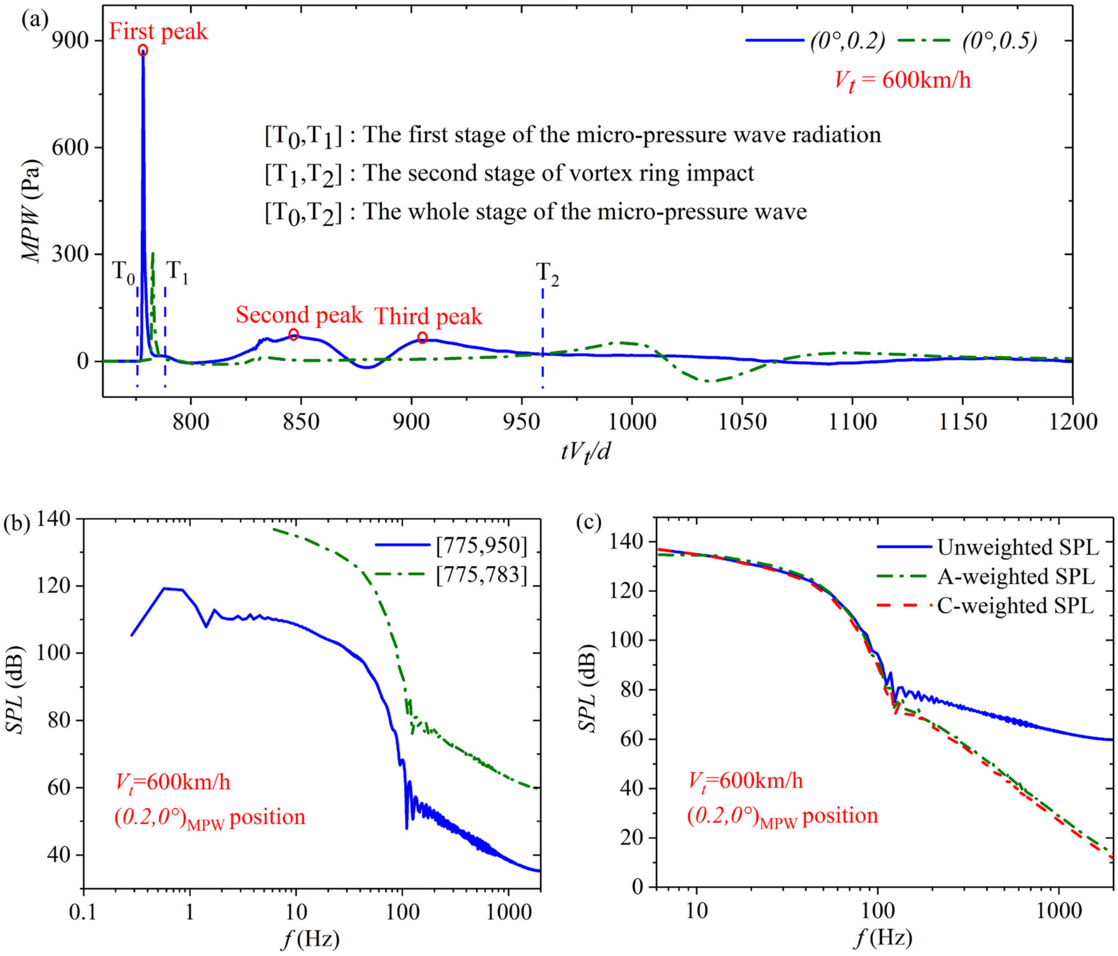

FIG. 19. Exploration of analytical methods for the spectral characteristics of MPW at 600 km/h train speed: (a) schematic diagram of radiation processes and vortex ring effects of MPW, (b) the spectral characteristics of MPW for the radiation and whole processes, and (c) the effect of unweighted, A-weighted, and C-weighted treatment on the spectral characteristics of MPW. The time interval [775, 950] represents [T0, T2], and the time interval [775, 783] represents [T0, T1]. The temporal MPW data of [775, 783] were utilized in the analysis of weighted effects.

Figure 22(c) demonstrates that the core diameter was most affected by the pinch-off process. The core diameter continuously thickened and deformed before the pinch-off process, and then narrowed when entered the disappearance stage after the pinch-off process. Figure 22(d) shows that the change trend of the ratio of the core diameter to the ring diameter was like that of the core diameter, and the overall value was less than 1, indicating that the current PCVR had a thin ring shape.[49]

Figure 23 displays the influence of vortex rings on the spectral characteristics of the axial MPW, with sampling times of [T_1, T_2]. The SPL gradually decreases with the increase in axis distance, and the lowest frequency also gradually decreases. Additionally, the vortex ring is sufficient to generate secondary noise at $V_t = 600$ km/h. However, the SPL of this noise is much smaller than the SPL of the sonic boom caused by the impulse waves. Therefore, both the effects of the impulse wave in the early stage and the vortex ring in the later-stage may generate potential noise in the analysis of MPW. The sonic boom caused by the impulse wave is the primary concern.

D. Noise protection discussion

Stronger levels of MPW can have negative effects on the health of residents and animals near tunnel portals. In addition to the loud sonic booms that can be heard, the low-frequency components of MPW can cause vibrations in building structures. To better understand the negative effects of MPW, it is necessary to discuss noise protection. European directive 2003/10/EC[27] provides clear regulations for C-weighted SPL peak values in the acoustic evaluation perspective. As listed in Fig. 1, for environments near tunnel portals, the lower exposure action value at $L_{pC,peak} = 135$ dB(C) should not be exceeded. Additionally, the C-weighted sound peak value $L_{pC,peak} = 115$ dB(C) at 25 m from the portal should not be exceeded. Limited by simulation

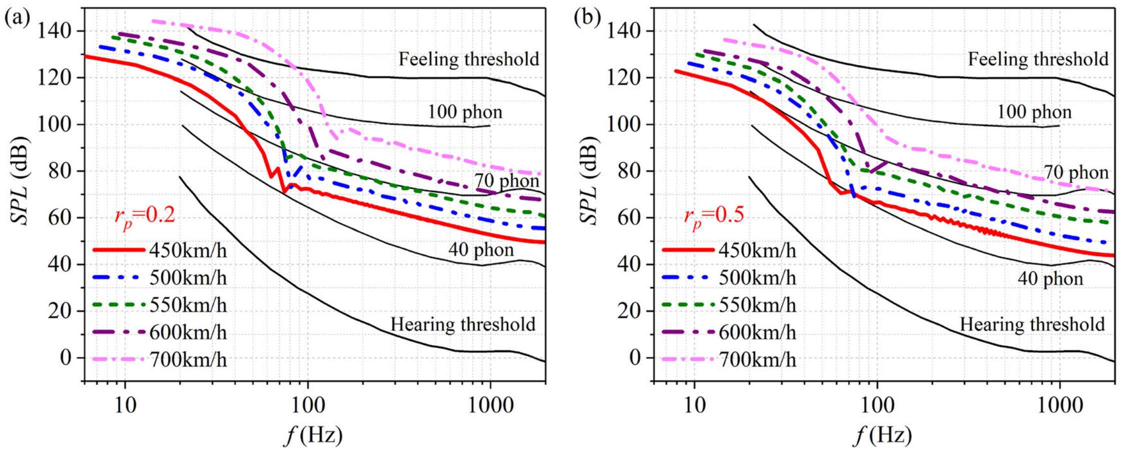

FIG. 20. Synthetic analysis of equal-loudness-level contours at different train speeds: (a) sound pressure level assessment at (0.2, 0)$_{MPW}$ position and (b) sound pressure level assessment at (0.5, 0)$_{MPW}$ position.

resource consumption, this study only considers MPW within a range of $r_p \leq 1$ m (full size of 97 m). Therefore, environmental indicators for buildings near tunnels are not analyzed.

Figure 24 shows the C-weighted SPL distribution at the (0.2, 0)$_{MPW}$ position and the (0.5, 0)$_{MPW}$ position at different speed levels. The $L_{pC,peak}$ distribution of the axial direction MPW is displayed in Fig. 25(a). Although the sound peak value corresponds to an infrasound range, the energy within this frequency still has a negative impact. Currently, the $L_{pC,peak}$ values of the axial MPW in the 450–700 km/h range are greater than 115 dB(C), and a small portion is greater than 135 dB(C). Furthermore, the C-weighted SPL distribution of the (0.25, 0)$_{MPW}$ position is presented in Fig. 25(b). Figure 25(b) indicates that the SPL at this position exceeds the threshold of 115 dB (C) in the 450–700 km/h range, and the frequency at which the threshold intersects with the SPL is greater than 20 Hz. This means that the MPW at the (0.25, 0)$_{MPW}$ position on the axis in the 450–700 km/h range will cause dual hazards of sonic booms and building structures resonances.

In addition to the acoustic standard, scholars usually use the single-point MPW amplitude standard for evaluation (as listed in Fig. 1). This study attempts to investigate the relationship between above two standards. Therefore, Fig. 26(a) demonstrates ten temporal MPWs along the axis at $V_t = 450$ km/h. While there are significant differences in amplitude among all waveforms, the durations of the impulse waves [T$_0$, T$_1$] are approximately equal to $tV_t/d = 6$. Using these temporal MPW curves as a database and without altering the trend of MPW, only their amplitudes are adjusted to 20 and 50 Pa. Based on this approach, Fig. 26(b) presents the reconstructed waveform 1 (20 Pa) and waveform 2 (50 Pa). Figures 26(c) and 26(d), respectively, represent the unweighted and C-weighted spectral characteristics of these two waveforms. The unweighted SPL of waveform 1 and waveform 2 both exceed the hearing threshold, but their loudness is relatively small. However, the C-weighted SPL of waveform 1 and waveform 2 are both less than the threshold of 115 dB(C). This discussion is beneficial for the subsequent development of MPW standards for maglev tube, to better achieve a reasonable balance between construction costs and environmental protection.

IV. CONCLUSION

The maglev train/tube coupling model was utilized to study the formation and propagation mechanism of the WSW in the tube within a speed range of 450–700 km/h. The two-dimensional axisymmetric URANS based on the SST k–ω turbulence model was adopted to solve the model. The fitting formula of the amplitude of the initial wavefront gradient was used to evaluate the formation distance of the WSW, and the physical parameters of the WSW were quantitatively described. The spatial and spectral characteristics of MPW and the influence of vortex rings on MPW were analyzed. Finally, the topic of noise protection related to MPW was discussed around the standards. The main research conclusions are summarized as follows.

i. The inertial effect causes the initial wavefront to gradually transit from a Gaussian-shape waveform to a triangular waveform during its propagating, eventually coalescing into a WSW. There are three regions along the tube where the wavefront gradient exists: before the WSW appears, the wavefront gradient continues to increase, reaching a maximum at the location of the WSW, and then the wavefront gradient decreases slightly and fluctuates.

ii. As the train speed increases, the overpressure, shock Mach number, and density jump of the WSW increase, while the thickness of the WSW decreases. The formation distance of the WSW can be theoretically evaluated by Eq. (9). L_s is inversely proportional to the initial wavefront gradient amplitude. When $\beta = 0.12$ and $V_t = 700$ km/h, the full-scale L_s has been reduced to an astonishing 0.57 km. Through the verification of sonic boom events, experimental data, and simulation data, Eq. (9) accurately predicts the L_s in a simple tube. This theoretical formula benefits for the conceptual design of the future maglev railway to keep away from the value of L_s.

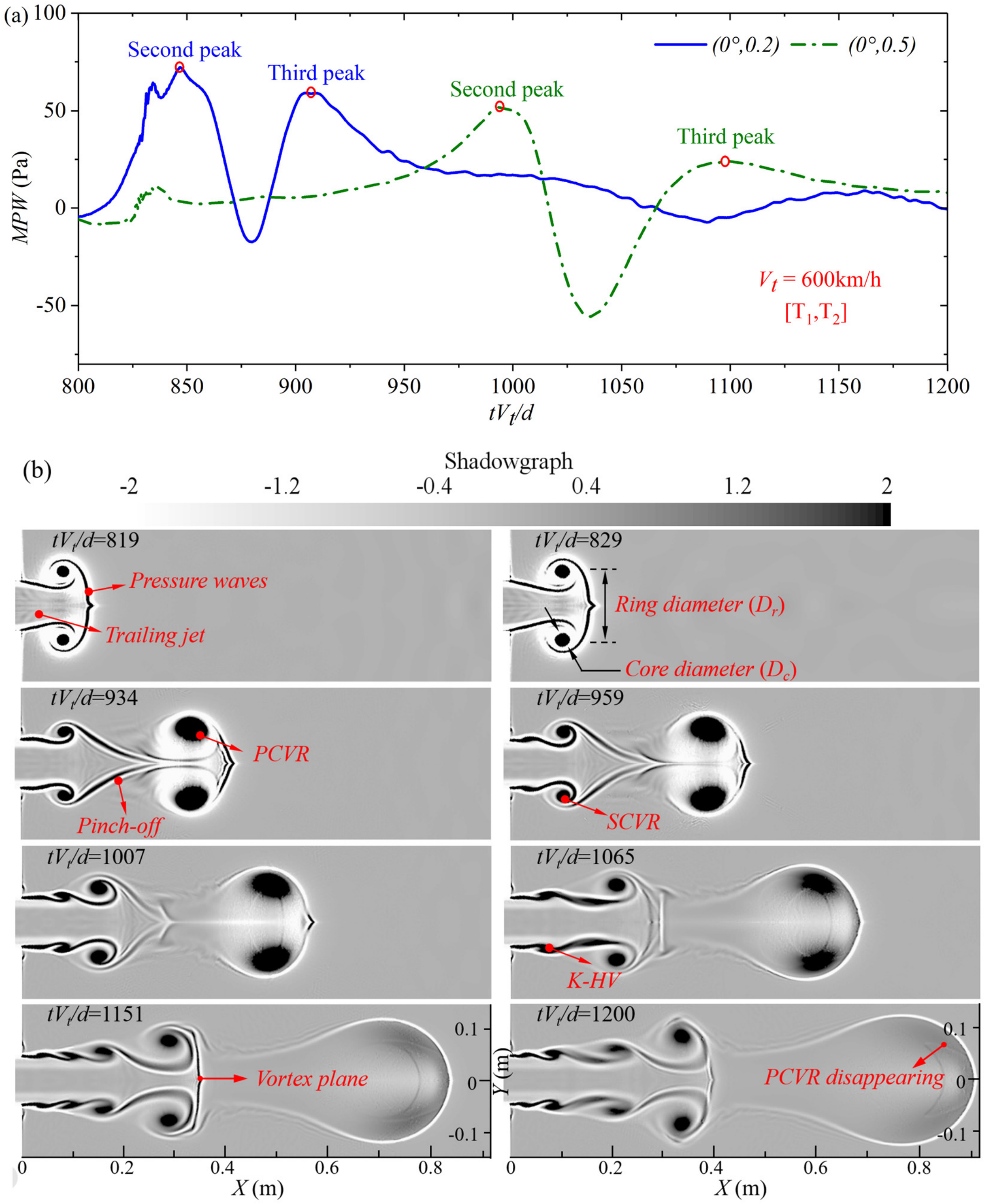

FIG. 21. Evolution of vortex rings and its influence on MPW at 600 km/h train speed: (a) the temporal pressure profiles of the MPW under the influence of the vortex rings and (b) the whole process of emergence, evolution, and disappearance of vortex rings.

iii. The MPW amplitude can be predicted by Eq. (11). The MPW amplitude is proportional to the train speed up to a power index of 4.39, and gradually decreases downstream along the axis. The maximum amplitude of MPW reaches 3.4×10^{-2} p^*, and the duration is only 1.7×10^{-3} s at the train speed of 700 km/h. By comparing with the equal-loudness-level contours, the sound pressure level of MPW has exceeded the hearing threshold. Therefore, it will inevitably be accompanied by a loud sonic boom when a WSW forms in the maglev tube and propagates to the tunnel exit at speed range of 450–700 km/h.

iv. MPW first radiates outward in a semi-ellipsoid shape, and then gradually transforms into a semi-sphere and propagates downstream. Therefore, the magnitude of MPW has significant directionality. The magnitude of axial MPW is the largest at the same

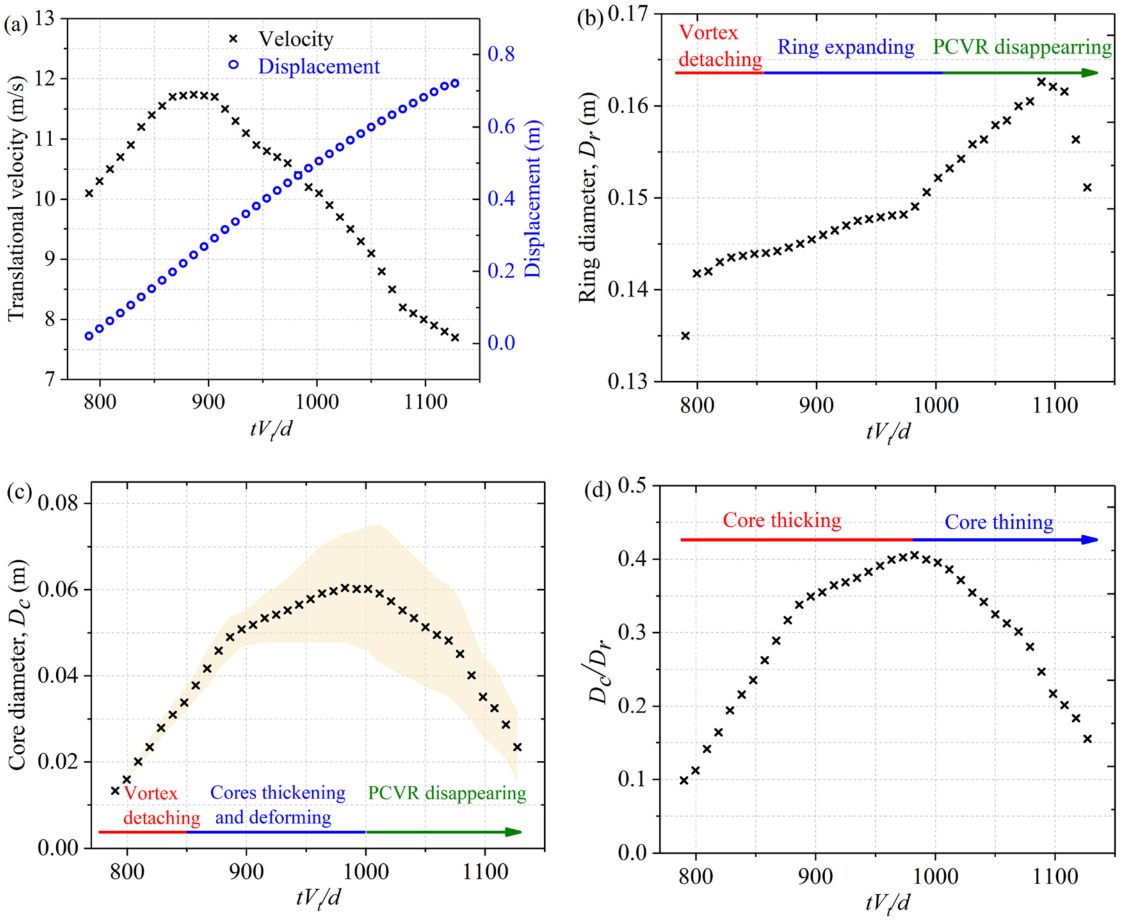

FIG. 22. Kinematic and geometric characteristics of PCVR at 600 km/h train speed: (a) the translational velocity and the displacement of the PCVR, (b) the evolution of the vortex ring diameter, (c) the evolution of the vortex core diameter, and (d) the ratio of the core diameter to the ring diameter.

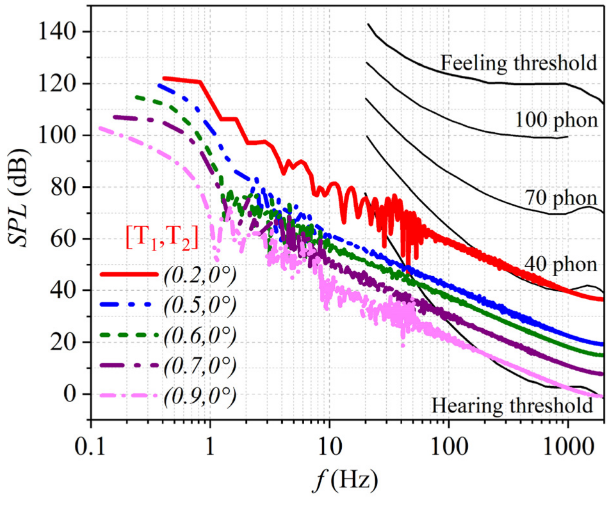

FIG. 23. Spectral characteristics of MPW along the flow direction under the influence of vortex ring at 600 km/h train speed.

radius, while the magnitude of MPW perpendicular to the axis decreases significantly, and this phenomenon further increases with the increase of train speed. However, the directivity of MPW was weakened as MPW propagates downstream.

v. The evolution of compressible vortex rings can be divided into four stages: rapid growth stage, pinch-off stage, free development stage, and disappearance stage. Compared to secondary compressible vortex rings and Kelvin–Helmholtz vortices, the primary compressible vortex rings have a greater impact on the axial MPW. The translational velocity, ring diameter, core diameter of the compressible vortex rings are described. The MPW fluctuations induced by the compressible vortex rings can cause noise with small amplitude.

vi. Within the speed range of 450–700 km/h, the sound pressure level at a specified location exceeds the threshold of 115 dB(C), and the frequency at which the threshold intersects with the sound pressure level is greater than 20 Hz. This means that the MPW at the specified location will cause the dual hazards of sonic boom and building structure resonance. Measures must be taken in the design of future maglev tube to mitigate the impact

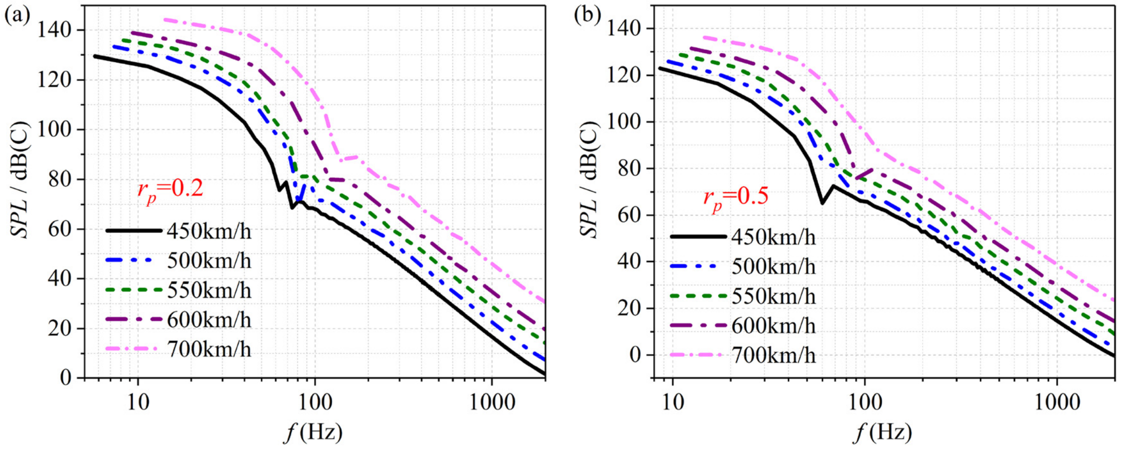

FIG. 24. C-weighted sound pressure level at different train speeds: (a) (0.2, 0)$_{MPW}$ position and (b) (0.5, 0)$_{MPW}$ position.

of MPW. The MPW standard needs to be developed combination with its acoustic characteristics to achieve the best cost-benefit balance.

Note that the relationship between WSW and aerodynamic drag of trains is also worth exploring. There are two common types of maglev trains: evacuated tube transport (ETT) and conventional maglev trains.[50] ETT trains usually gradually accelerate to supersonic speeds within a closed tube. The ideal speed of maglev trains is 0.5M, and it is common for trains to traverse tunnels. During the process of ETT trains gradually accelerating to supersonic speeds, there are three inflection points in aerodynamic drag.[34] The first inflection point occurs before the onset of choked flow, where the growth rate of aerodynamic drag is high and aerodynamic drag continuously increases. When the train's tail exhibits a fully expanded flow state, the second inflection point appears, at which point the increase rate in aerodynamic drag decreases. The third inflection point occurs in the supersonic state of the train, where the forward normal shock wave of the train transforms into an oblique shock wave attached to the train. Correspondingly, the choked flow is fully dissipated, resulting in a significant reduction in aerodynamic drag.[34,51] In the case of maglev tube, WSW is typically present in front of the train. WSW may encounter the train and cause changes in its aerodynamic drag only when they reflect as expansion waves at the tube exit. Therefore, we focus on the relationship between WSW and tube exit sonic booms in the current study, while downplaying the discussion of aerodynamic drag. The relationship between WSW and aerodynamic drag of trains will be an important research content for future investigations.

From the foregoing content, the MPW amplitude and MPW sound pressure level of the maglev tube without hood at $V_t = 600$ km/h have far exceeded the threshold. Therefore, reasonable measures must be taken to avoid the occurrence of sonic boom at the tube exit. Mitigation measures involve both the design of the train's exterior and the transformation of the tunnel. The exterior design of the train can

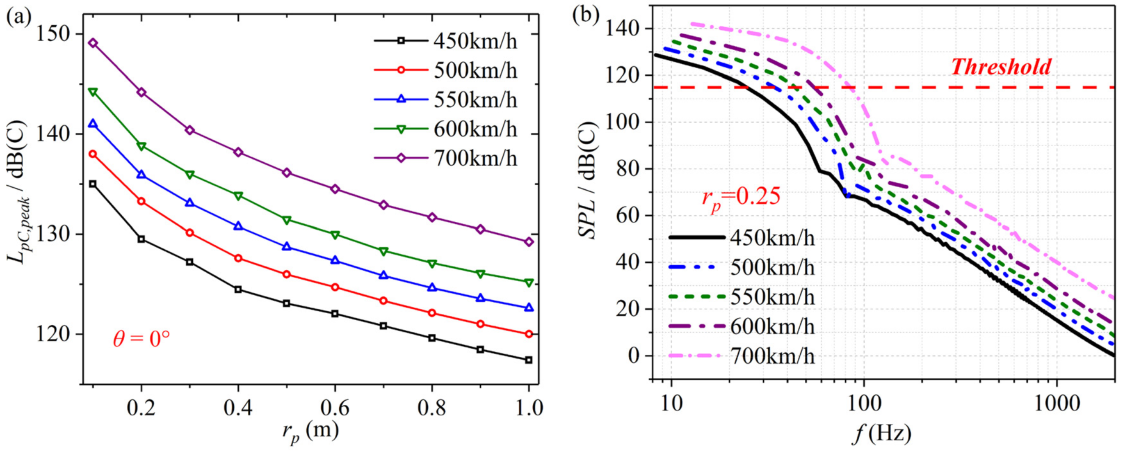

FIG. 25. Noise protection assessment near the portal environment: (a) C-weighted sound peak level distribution along the flow direction at different train speeds and (b) threshold evaluation at (0.25, 0)$_{MPW}$ position.

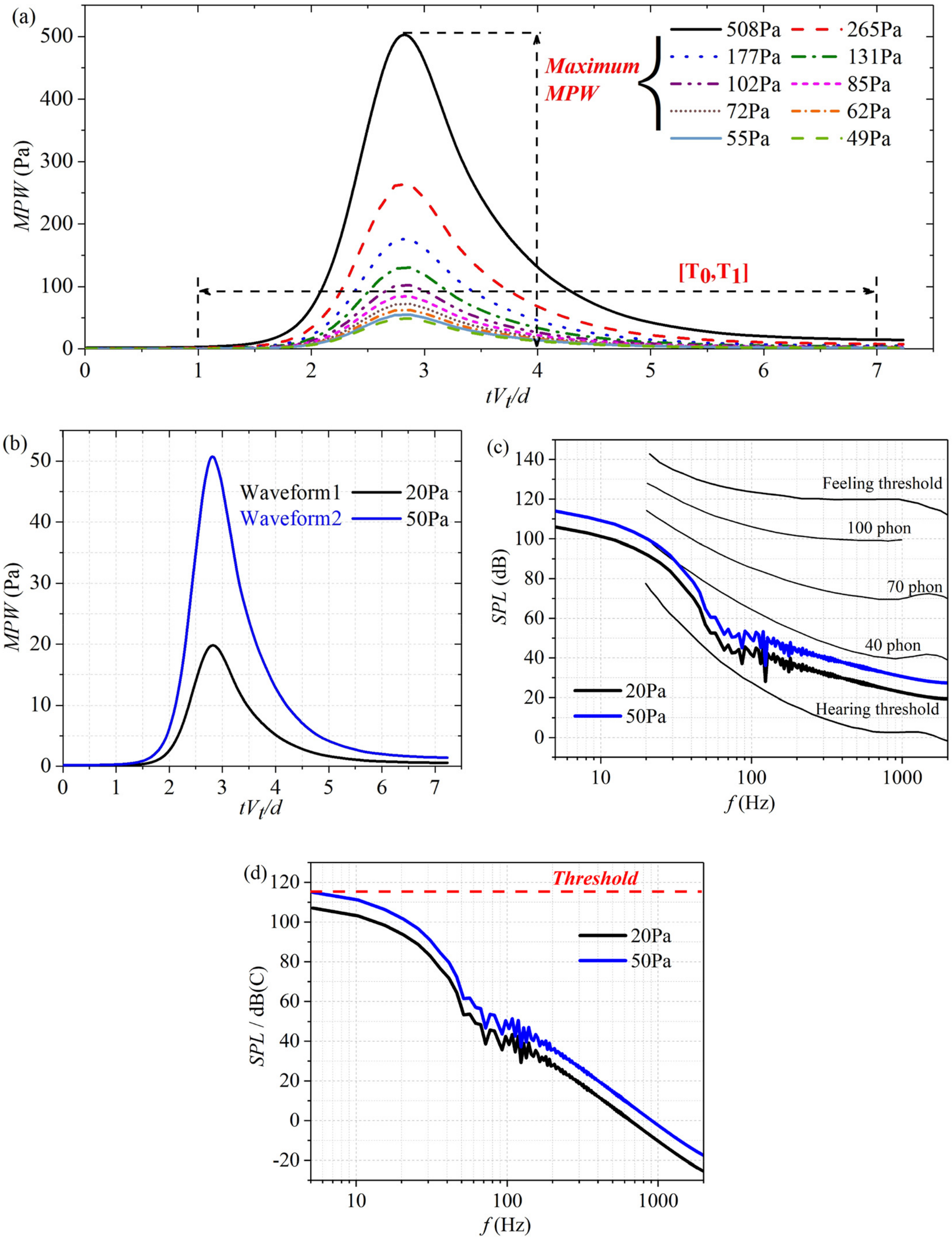

FIG. 26. Comprehensive comparison of impulse amplitude standard and acoustic criterion: (a) the waveform database of MPW, (b) MPW waveforms constructed with two standard thresholds, (c) spectrum distribution of two waveforms combined with the equal-loudness-level contours, and (d) C-weighted sound pressure level combined with the acoustic criterion.

further apply bionics to the head design, further explore multistep train nose, and clarify the reasonable cross-sectional area of the train and the tunnel. However, the structural transformation of the tunnel seems to have a more significant effect on the mitigation of MPW. For example, installing novel vented hoods at the tunnel portals,[52,53] setting up reasonable airshafts, installing a series of Helmholtz resonators along the tunnel,[54] and installing sound-absorbing plates near the tracks[55] are all methods worth investigating.

ACKNOWLEDGMENTS

The authors acknowledge the computational resources provided by the High-Performance Computing Center of Central South University, China. This work was supported by the National Key R & D program of China (Grant No. 2020YFA0710903) and the Natural Science Foundation of Hunan Province (Grant No. 2021JJ30849).

AUTHOR DECLARATIONS

Conflict of Interest

The authors have no conflicts to disclose.

Author Contributions

Kai-Wen Wang: Conceptualization (equal); Data curation (equal); Formal analysis (equal); Software (equal); Validation (equal); Visualization (equal); Writing – original draft (equal). **Xiao-Hui Xiong:** Conceptualization (equal); Funding acquisition (equal); Supervision (equal); Validation (equal). **Chih-Yung Wen:** Conceptualization (equal); Formal analysis (equal); Writing – review & editing (equal). **Guang Chen:** Conceptualization (equal); Formal analysis (equal); Validation (equal); Writing – review & editing (equal). **Xi-Feng Liang:** Conceptualization (equal); Funding acquisition (equal). **Hua-Kun Huang:** Formal analysis (equal); Software (equal); Validation (equal); Writing – review & editing (equal). **Jia-Bin Wang:** Conceptualization (equal); Software (equal); Writing – review & editing (equal).

DATA AVAILABILITY

The data that support the findings of this study are available from the corresponding author upon reasonable request.

REFERENCES

[1] H. Kwon, Y. Jin, W. Lee, and H. Kang, "The feasibility of adapting air compressor to a high-speed train to attenuate the aerodynamic problems in tunnel," Int. J. Aeronaut. Space Sci. **21**(3), 638–646 (2020).

[2] D. Uystepruyst, M. William-Louis, E. Creusé, S. Nicaise, and F. Monnoyer, "Efficient 3D numerical prediction of the pressure wave generated by high-speed trains entering tunnels," Comput. Fluids **47**(1), 165–177 (2011).

[3] G. Zhang, T. H. Kim, D. H. Kim, and H. D. Kim, "Prediction of micro-pressure waves generated at the exit of a model train tunnel," J. Wind Eng. Ind. Aerodyn. **183**(8), 127–139 (2018).

[4] C. Gerbig and K. G. Degen, "Acoustic assessment of micro-pressure wave emissions from high-speed railway tunnels," in *Noise and Vibration Mitigation for Rail Transportation Systems*, Notes on Numerical Fluid Mechanics and Multidisciplinary Design Vol. 118 (Springer, 2010), pp. 389–396.

[5] S. Sepúlveda Abad, "Influence of aerodynamics in tunnels design," in *International Congress on High-Speed Rail: Technologies and Long Term Impacts* (University of Castilla La Mancha, 2018), pp. 333–353.

[6] B. Auvity and M. Bellenoue, "Effects of an opening on pressure wave propagation in a tube," J. Fluid Mech. **538**, 269–289 (2005).

[7] M. Hieke, K. Hans-Jakob, and T. Tielkes, "Prediction of micro-pressure wave emissions from high-speed railway tunnels," in *Proceedings of 13th International Symposium on Aerodynamics and Ventilation of Vehicle Tunnels* (BHR Group, 2009), pp. 487–503.

[8] Z. Chen, Z. Guo, Y. Ni, T. Liu, and J. Zhang, "A suction method to mitigate pressure waves induced by high-speed maglev trains passing through tunnels," Sustainable Cities Soc. **96**(5), 104682 (2023).

[9] S. Han, J. Zhang, X. H. Xiong, P. Ji, L. Zhang, J. Sheridan, and G. J. Gao, "Influence of high-speed maglev train speed on tunnel aerodynamic effects," Build. Environ. **223**(8), 109460 (2022).

[10] A. Sasoh, *Compressible Fluid Dynamics and Shock Waves* (Springer, Nagoya, Japan, 2020).

[11] P. Derkowski, S. Clark, R. Sturt, A. Keylin, C. Baker, A. Vardy, and N. Wilson, "High-speed rail aerodynamic assessment and mitigation report," Report No. DOT/FRA/ORD-15/40, 2015.

[12] K. Takayama, A. Sasoh, O. Onodera, R. Kaneko, and Y. Matsui, "Experimental investigation on tunnel sonic boom," Shock Waves **5**(3), 127–138 (1995).

[13] J. M. Rivero, E. González-Martínez, and M. Rodríguez-Fernández, "A methodology for the prediction of the sonic boom in tunnels of high-speed trains," J. Sound Vib. **446**, 37–56 (2019).

[14] H. Wang, B. Lei, H. Bi, and T. Yu, "Wavefront evolution of compression waves propagating in high speed railway tunnels," J. Sound Vib. **431**, 105–121 (2018).

[15] R. S. Iyer, D. H. Kim, and H. D. Kim, "Propagation characteristics of compression wave in a high-speed railway tunnel," Phys. Fluids **33**(8), 086104 (2021).

[16] J. Zhang, B. Guo, Y. Wang, S. Han, X. Xiong, S. Krajnović, and G. Gao, "A novel vented tunnel hood with decreasing open ratio to mitigate micro-pressure wave emitted at high-speed maglev tunnel exit," J. Wind Eng. Ind. Aerodyn. **240**(5), 105459 (2023).

[17] J. Zhang, Y. Wang, S. Han, F. Wang, and G. Gao, "A novel arch lattice-shell of enlarged cross-section hoods for micro-pressure wave mitigation at exit of maglev tunnels," Tunnelling Underground Space Technol. **132**(7), 104859 (2023).

[18] T. Miyachi, K. Kikuchi, and M. Hieke, "Multistep train nose for reducing micro-pressure waves," J. Sound Vib. **520**(10), 116665 (2022).

[19] A. E. Vardy, "Generation and alleviation of sonic booms from rail tunnels," Proc. Inst. Civ. Eng. **161**(3), 107–119 (2008).

[20] A. E. Vardy and J. M. B. Brown, "Influence of ballast on wave steepening in tunnels," J. Sound Vib. **238**(4), 595–615 (2000).

[21] T. Miyachi, T. Fukuda, M. Iida, T. Maeda, and S. Ozawa, "Distortion of compression wave propagating through Shinkansen tunnel," in *Noise and Vibration Mitigation for Rail Transportation Systems*, Notes on Numerical Fluid Mechanics and Multidisciplinary Design Vol. 99 (Springer, 2008), pp. 9–18.

[22] S. Adami and H.-J. Kaltenbach, "Sensitivity of the wave-steepening in railway tunnels with respect to the friction model," in *6th International Colloquium on Bluff Body Aerodynamics and Applications, 20–24 July* (International Association on Wind, 2008).

[23] T. Miyachi, "Acoustic model of micro-pressure wave emission from a high-speed train tunnel," J. Sound Vib. **391**, 127–152 (2017).

[24] H. Wang, A. E. Vardy, and D. Pokrajac, "Pressure radiation from a perforated duct exit region," J. Sound Vib. **351**(5), 29–42 (2015).

[25] H. Wang, A. E. Vardy, and H. Bi, "Characteristics of pressure waves radiated from tunnel portals in cuttings," J. Sound Vib. **521**(10), 116664 (2022).

[26] L. Zhang, M. Yang, X. Liang, and J. Zhang, "Oblique tunnel portal effects on train and tunnel aerodynamics based on moving model tests," J. Wind Eng. Ind. Aerodyn. **167**(8), 128–139 (2017).

[27] The European Parliament and of the Council, "Minimum health and safety requirements regarding the exposure of workers to the risks arising from physical agents (noise)," European Directive 2003/10/EC, 2003.

[28] Y. Suzuki and H. Takeshima, "Equal-loudness-level contours for pure tones," J. Acoust. Soc. Am. **116**(2), 918–933 (2004).

[29] J. J. P. Fernández and J. Sesterhenn, "Compressible starting jet: Pinch-off and vortex ring-trailing jet interaction," J. Fluid Mech. **817**, 560–589 (2017).

[30] H. Ahmad, N. Hasan, and S. Sanghi, "On the influence of co-flow on the shocks and vortex rings in the starting phases of under-expanded jets," Phys. Fluids **34**(7), 076117 (2022).

[31] Y. Xiang, L. Qin, S. Qin, and H. Liu, "Circulation production model and unified formation number of compressible vortex rings generated by a shock tube," Phys. Fluids **35**(3), 036121 (2023).

[32] T. Murugan, S. De, C. L. Dora, and D. Das, "Numerical simulation and PIV study of compressible vortex ring evolution," Shock Waves **22**(1), 69–83 (2012).

[33] S. Saito, M. Iida, and H. Kajiyama, "Numerical simulation of 1-D unsteady compressible flow in railway tunnels," J. Environ. Eng. **6**(4), 723–738 (2011).

[34] S. Zhong, M. Yang, B. Qian, T. Wang, F. Wu, and L. Zhang, "Temporal evolution of flow field structure for vehicles accelerating in evacuated tube transportation system," Phys. Fluids **35**(2), 025117 (2023).

[35] T. Mrazek, Y. Sato, M. A. Sayed, and N. Nick, "Investigation of shock waves reflected at the end of a Hyperloop tube," Aerosp. Sci. Technol. **139**(5), 108379 (2023).

[36] G. Chen, X. Li, R. Xue, K. He, H. Wang, and X. Liang, "Effects of incoming free-stream turbulence on the flow dynamics of a square finite wall-mounted cylinder," Phys. Fluids **35**(2), 025140 (2023).

[37] T. Maeda, T. Matsumura, M. Iida, K. Nakatani, and K. Uchida, "Effect of shape of train nose on compression wave generated by train entering tunnel," in *The International Conference on Speedup Technology for Railway and Maglev Vehicles* (The Japan Society of Mechanical Engineers, 1993), pp. 315–319.

[38] M. Wu and M. P. Martin, "Direct numerical simulation of supersonic turbulent boundary layer over a compression ramp," AIAA J. **45**(4), 879–889 (2007).

[39] T. Tamba, G. Fukushima, M. Kayumi, A. Iwakawa, and A. Sasoh, "Experimental investigation of the interaction of a weak planar shock with grid turbulence in a counter-driver shock tube," Phys. Rev. Fluids **4**(7), 073401 (2019).

[40] J. Varnier, M. C. Le Pape, and F. Sourgen, "Ballistic wave from projectiles and vehicles of simple geometry," AIAA J. **56**(7), 2725–2742 (2018).

[41] M. S. Howe, M. Iida, T. Fukuda, and T. Maeda, "Theoretical and experimental investigation of the compression wave generated by a train entering a tunnel with a flared portal," J. Fluid Mech. **425**, 111–132 (2000).

[42] M. Bellenoue, V. Morinière, and T. Kageyama, "Experimental 3-D simulation of the compression wave, due to train-tunnel entry," J. Fluids Struct. **16**(5), 581–595 (2002).

[43] C. Wang, *Research on the Propagation Characteristics of Air Pressure Waves and Mitigation Measures for Micro Pressure Waves in High Speed Railway Tunnels* (China Academy of Railway Sciences, 2023).

[44] R. Yamashita and H. Ishikawa, "A semi-adapted space marching method for fast sonic boom prediction," J. Comput. Phys. **487**, 112170 (2023).

[45] G. Zhang, D. H. Kim, and H. D. Kim, "Numerical studies on the radiation of train-tunnel impulse waves," Tunnelling Underground Space Technol. **80**(7), 211–221 (2018).

[46] L. Qin, Y. Xiang, H. Lin, and H. Liu, "Formation and dynamics of compressible vortex rings generated by a shock tube," Exp. Fluids **61**(3), 86 (2020).

[47] C. L. Dora, T. Murugan, S. De, and D. Das, "Role of slipstream instability in formation of counter-rotating vortex rings ahead of a compressible vortex ring," J. Fluid Mech. **753**, 29–48 (2014).

[48] S. Poudel, L. Chandrala, D. Das, and A. De, "Characteristics of shock tube generated compressible vortex rings at very high shock Mach numbers," Phys. Fluids **33**(9), 096105 (2021).

[49] C. Xiong, Z. Wang, and X. Huang, "Blow-off of diffusion flame by moving air vortex ring," Exp. Therm. Fluid Sci. **151**(9), 111059 (2024).

[50] Z. Hou, Y. Zhu, J. Bo, and J. Yang, "A quasi-one-dimensional study on global characteristics of tube train flows," Phys. Fluids **34**(2), 026104 (2022).

[51] Z. Zhou, C. Xia, X. Du, X. Shan, and Z. Yang, "Impact of the isentropic and Kantrowitz limits on the aerodynamics of an evacuated tube transportation system," Phys. Fluids **34**(6), 066103 (2022).

[52] D. H. Kim, S. Y. Cheol, R. S. Iyer, and H. D. Kim, "A newly designed entrance hood to reduce the micro pressure wave emitted from the exit of high-speed railway tunnel," Tunnelling Underground Space Technol. **108**(10), 103728 (2021).

[53] T. Miyachi and T. Fukuda, "Model experiments on area optimization of multiple openings of tunnel hoods to reduce micro-pressure waves," Tunnelling Underground Space Technol. **115**(6), 103996 (2021).

[54] F. Liu, A. E. Vardy, and D. Pokrajac, "Influence of air chambers on wavefront steepening in railway tunnels," Tunnelling Underground Space Technol. **117**(7), 104120 (2021).

[55] T. Fukuda, S. Nakamura, T. Miyachi, S. Saito, N. Kimura, and M. Matsunuma, "Influence of ballast quantity on compression wavefront steepening in railway tunnels," Proc. Inst. Mech. Eng., Part F **234**(6), 607–615 (2020).